THE FLORIDA STATE UNIVERSITY

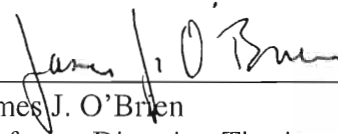COLLEGE OF ARTS AND SCIENCES

INTERANNUAL VARIABILITY OF UPPER OCEAN VORTICITY BALANCES

IN THE GULF OF ALASKA

By

COLIN PATRICK MURRAY

A thesis submitted to the
Department of Oceanography
in partial fulfillment of the
requirements for the degree of
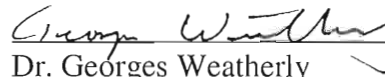Master of Science

Degree Awarded:
Fall Semester, 1999

The members of the Committee approve the thesis of Colin P. Murray defended on July 30, 1999.

_____
James J. O'Brien
Professor Directing Thesis

_____
Dr. Georges Weatherly
Committee Member

_____
Dr. Richard Iverson
Committee Member

ACKNOWLEDGEMENTS

TABLE OF CONTENTS

LIST OF FIGURES

ABSTRACT

A high-resolution numerical ocean model is used to examine the interannual variability of upper ocean vorticity balances in the Gulf of Alaska. A circulation equation is derived for a layer representative of the upper ocean. The equation compares the surface integral of vorticity over the domain of the layer with time-integrated vorticity flow through the layer boundaries. Time series of vorticity transport through each pathway are constructed and examined for interannual variability. Other native and derived model variables are analyzed to facilitate explanation of observed interannual variability.

The model data show that interannual variability in the circulation of the Gulf of Alaska is negligible relative to its mean. However, the sources and sinks that feed and drain vorticity from the region do vary interannually, and the variation is predominantly due to atmospheric and oceanic teleconnections originating with the El Niño-Southern Oscillation. The amount of vorticity injected into the upper ocean by the wind stress curl is reduced during the early phase of El Niño events by the weakening of the Aleutian Low [*Emery and Hamilton*, 1985; *Putman*, 1998]. El Niño events also excite poleward-traveling downwelling coastal Kelvin waves that propagate up the eastern continental margin of the northeast Pacific Ocean [*Meyers et al.*, 1998]. These waves strengthen the Alaska Current at the peak of its annual cycle, triggering baroclinic instabilities which margin of the northeast Pacific Ocean [*Meyers et al.*, 1998]. These waves strengthen the Alaska Current at the peak of its annual cycle, triggering baroclinic instabilities which result in the formation of a coast-wide train of anticyclonic eddies [*Melsom et al.*, 1995;

1998]. The more southerly of these eddies tend to propagate to the southwest, carrying

negative vorticity out of the Gulf of Alaska. This net gain of vorticity is inversely

correlated with and serves to balance the nearly contemporaneous reduction of vorticity

input by the wind stress curl. Due to the baroclinic nature of both the eddies and the

influence of the wind stress curl, the effect is largely confined to the upper ocean.

1. INTRODUCTION

The Alaskan Gyre is the most prominent oceanographic feature in the Gulf of Alaska. (Figure 1) It is approximately bounded on the south by the eastward flowing Pacific Current ($\sim 45^o N$), which separates at the continental margin into the southward-flowing California Current and the poleward-flowing Alaska Current. The latter current ambles northwestward until it curves around the southern coast of Alaska and accelerates west of Kodiak Island, becoming the Alaskan Stream. The timing and position of recirculation filaments connecting the Alaskan Stream to the Pacific Current vary according to local wind stress curl [*Thomson*, 1972].

The cyclonic mean circulation of the gyre is wind-driven. The peak of the annual cycle occurs during winter when the cyclonic Aleutian Low dominates the overlying atmospheric circulation. This pattern transitions every summer to one dominated by the north Pacific subtropical high.

Emery and Hamilton [1985] and *Putman* [1998] have examined interannual variability in the north Pacific atmospheric circulation and found a strong correlation with the El Niño-Southern Oscillation. The variability is manifest as a weakening of the Aleutian Low in the winter prior to an El Niño followed by a rapid restrengthening during its mature phase. Tropically-forced coastal Kelvin waves excited during El Niño events propagate up the eastern continental margin of the northeast Pacific Ocean and mature phase. Tropically-forced coastal Kelvin waves excited during El Niño events propagate up the eastern continental margin of the northeast Pacific Ocean and destabilize the Alaska Current, generating trains of large anticyclonic eddies. [*Melsom et*

1
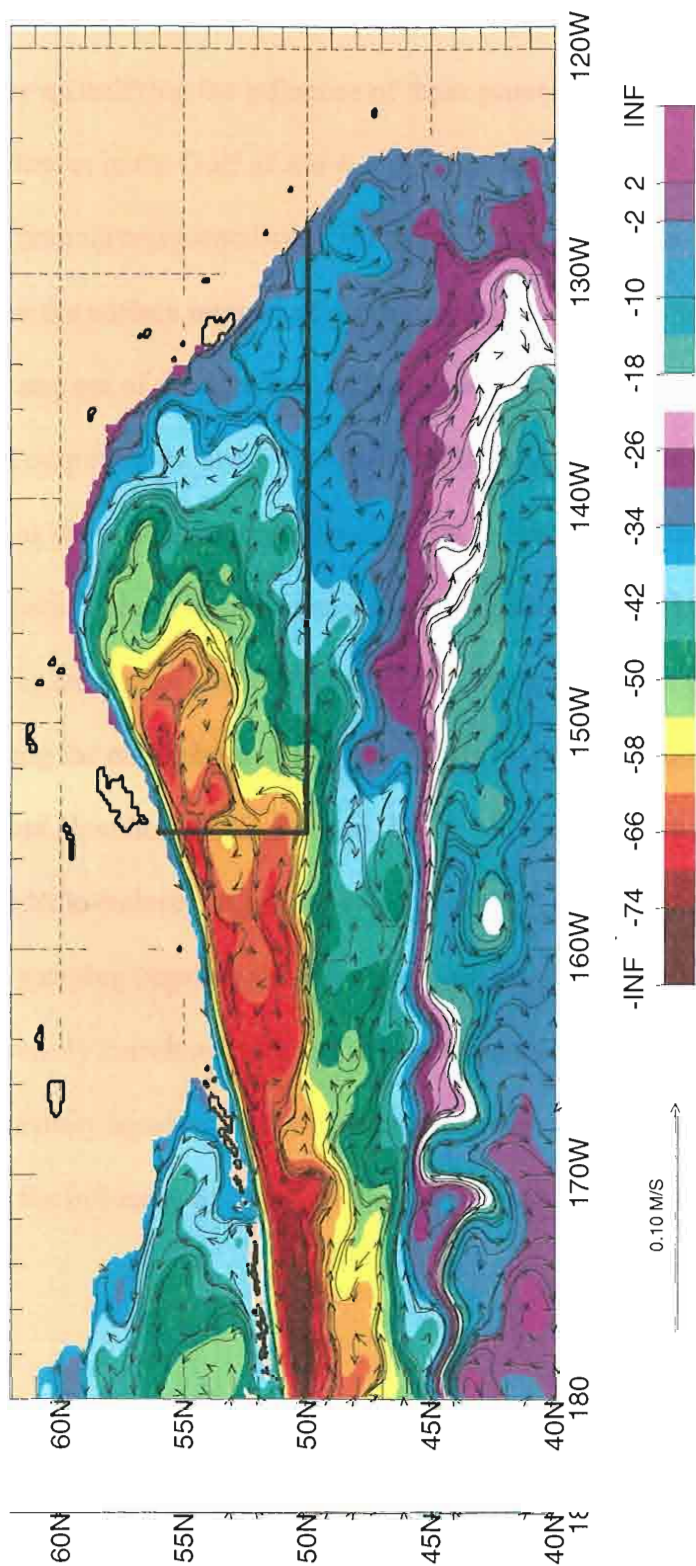
FIGURE 1: Mean annual currents and free surface deviation in meters for layer 1 in the northeast Pacific Ocean. The black lines demarcate the southern and western boundaries of the study region.

2

al., 1995; 1998] The interannual appearance of these eddies in the Gulf of Alaska is an important aspect of the upper ocean circulation. The present study extends these observations by quantifying the influence of these processes in the interannual variability of vorticity balances in the Gulf of Alaska. A circulation equation is derived and evaluated in a domain representative of the upper ocean in the Gulf of Alaska. The equation relates the surface integral of depth-averaged vorticity to vorticity flow through pathways into and out of the domain. A discretized version of the equation is solved with gridded model output fields, and a time series of the solution of each term constructed.

The solutions show that interannual variability in vorticity balances is predominantly due to atmospheric and oceanic teleconnections originating with the El Niño-Southern Oscillation. The amount of vorticity injected into the upper ocean by the wind stress curl is reduced during the early phase of El Niño events by the weakening of the Aleutian Low [*Emery and Hamilton,* 1985; *Putman,* 1998]. The more southerly of the eddies spawned by El Niño-induced tropically-forced coastal Kelvin waves tend to propagate to the southwest, carrying negative vorticity out of the Gulf of Alaska. This net gain of vorticity is inversely correlated with and serves to balance the nearly contemporaneous reduction of vorticity input by the wind stress curl. Due to the baroclinic nature of both the eddies and the influence of the wind stress curl, the effect is largely confined to the upper ocean.

2. THE OCEAN MODEL

2.1 Model Phenomenology

The Navy Layered Ocean Model (NLOM) is used for this project in order to better extend and complement preceding lower-resolution modeling studies of the Gulf of Alaska [*Melsom et al.*, 1995; *Melsom et al.*, 1998]. The NLOM is the primary isopycnal ocean model used for simulation of open-ocean circulation at the Naval Research Laboratory, Stennis Space Center, MS (NRLSSC). The latest version, described in *Wallcraft* [1991], is a descendant of the primitive equation model developed by *Hurlburt and Thompson* [1980]. Although both hydrodynamic and thermodynamic versions of the model are available, the most temporally useful data set available at the time of this research was hydrodynamic. The vertically integrated nonlinear model equations of motion for an *n*-layer hydrodynamic, finite depth model are, for $k = 1...n$:

$$\frac{\partial \vec{V}_k}{\partial t} + (\nabla \bullet \vec{V}_k + \vec{V}_k \bullet \nabla)\vec{v}_k + \hat{k} \times f\vec{V}_k =$$

$$-h_k \sum_{l=1}^{n} G_{kl} \nabla (h_l - H_l) +$$

$$\max(0, \omega_k)\vec{v}_{k+1} - (\max(0, -\omega_k) + \max(0, \omega_{k-1}))\vec{v}_k +$$

$$\max(0, -\omega_{k-1})\vec{v}_{k-1} +$$

$$\frac{\vec{\tau}_{k-1} - \vec{\tau}_k}{\max(0, -\omega_{k-1})}v_{k-1}^h \nabla^2 \vec{v} +$$

$$\frac{\vec{\tau}_{k-1} - \vec{\tau}_k}{\rho_0} + A_H h_k \nabla^2 \vec{v}_k$$

$$\frac{\partial h_k}{\partial t} + \nabla \bullet \vec{V}_k = \omega_k - \omega_{k-1}$$

See Appendix A for descriptions of variables and parameters.

The finite difference discretization of these equations is done on a C-grid. The grid spacing of variable fields is constant in latitude and longitude, resulting in higher zonal resolution at higher latitudes. See *Messinger and Arakawa* [1976] for a detailed discussion of numerical grids. A semi-implicit time scheme is used in the finite-depth formulation of the model. Both versions have a free surface and no-slip and kinematic boundary conditions. The finite-depth version includes the barotropic mode. See *Wallcraft* [1991] and *Hurlburt and Thompson* [1980] for a more complete discussion of model structure and implementation.

NRLSSC has made available model results from NLOM experiment P134-1.7. It is a fifteen-year six-layer finite-depth simulation integrated from January 1981 to December 1995. The data consist of velocity and layer thickness values for each layer at 3.05 day intervals and the wind stress fields with which the model was forced. Although the model is integrated on a C-grid, when saved, velocity data is interpolated onto the h grid for convenience. Wind stress fields are still co-located on u and v grids.

The model domain contains the central and northern Pacific Ocean extending zonally from $109.125^o E$ to $77.203135^o W$ and meridionally from $20.0^o S$ to $62.0^o N$. No port is included for the Indonesian throughflow, hence there is no thermohaline circulation. However, the choice of domain does allow equatorially-generated coastal Kelvin waves to influence the northeast Pacific Ocean. Horizontal resolution is $1/16^o$ latitude by

$45/512^o$ longitude, which translates to a mean zonal spacing between like gridpoints in the Gulf of Alaska of about 7 *km*.

Realistic bathymetry and coastline geometry are included by using an NRLSSC improved version of the $1/12^o$ ETOP05 data set [*NOAA*, 1986]. After interpolation to the $1/16^o$ model grid, the bathymetry is filtered twice with a nine-point smoother to minimize energy generation at scales poorly resolved by the model [*Leonardi*, 1998]. The model coastline is chosen at the 200 *m* isobath, a typical value for the shelf break. This is done to obviate difficulties arising from the necessity that bottom topography be confined to the lowest layer. In addition, the amplitude of the bathymetry is scaled by 0.8 in order to ensure that no bottom features protrude from the lowest layer during the course of the integration.

Layer thicknesses and densities are chosen to be optimally consistent with the [*Levitus*, 1982] ocean climatology across the model domain. (Table 1) Although these values are more than adequate to prevent layer surfacing or isopycnal outcropping (the diminution of layer thickness to zero) near the equator, problems can arise in subarctic areas. The model solves this problem by invoking a "hydromixing" scheme when a layer depth h_k falls below a predetermined entrainment thickness h_k^+. Mass and momentum from the layer below are entrained into the affected region of the surfacing layer. However, layer density values do not change, and in order to conserve mass in each layer, detrainment from the surfacing layer to the layer below occurs somewhere else (where there is no isopycnal outcropping) in the domain. See *Shriver and Hurlburt* [1997] for a detrainment from the surfacing layer to the layer below occurs somewhere else (where there is no isopycnal outcropping) in the domain. See *Shriver and Hurlburt* [1997] for a more detailed discussion.

6

Applied wind stress fields are the only forcing in this experiment. The hybrid ECMWF/HR wind stress data set is used. It is constructed by removing the 1981-1995 climatological mean from pseudo-stresses derived from the 1000 *mb* European Center for Medium-Range Weather Forecasts twelve-hourly winds and replacing it with that of the *Hellerman and Rosenstein* [1983] data set. The pseudo-stress fields are converted to stress fields by multiplication with the product of the drag coefficient, C_D, and the sea level density of air, ρ_{air}.

Initial conditions are obtained by interpolating a snapshot of the oceanic state from a previous lower resolution experiment onto the $1/16^o$ grid. The experiment is then spun up to statistical equilibrium by forcing with the HR monthly mean wind stress climatology. After statistical equilibrium is reached, forcing begins on 17 January 1981 with the twelve-hourly ECMWF/HR wind stress data set. The stress fields are linearly interpolated during calculation to the twelve-minute increments of the model time step.

.

TABLE 1: Parameters for Experiment P134-1.7

Parameter	Definition	Value
C_b	Coefficient of bottom friction	2×10^{-3}
C_d	Drag coefficient	1.5×10^{-3}
C_k	Coefficient of interfacial friction	0
g	Acceleration due to gravity	$9.80\ m\ s^{-2}$
h_k^+	k-th layer thickness at which entrainment starts	50 m ($k = 1,2$) 40 m ($k = 3$-6)
h_k^-	k-th layer thickness at	Set to a large and
h_k^+	k-th layer thickness at which entrainment starts	50 m ($k = 1,2$) 40 m ($k = 3$-6)
h_k^-	k-th layer thickness at which detrainment starts	Set to a large and unreachable number: (9999.0 m)

7

TABLE 1 -- continued

Parameter	Definition	Value
$\tilde{\omega}_k$	k-th interface reference vertical mixing velocity	$0.04\ m\ s^{-1}$
TOPAMP	Bathymetry reduction factor	0.80
ρ_{air}	Sea-level air density	$1.2\ kg\ m^{-3}$
ρ_k	Density of layer k Sigma-T	$23.95\ kg\ m^{-3}\ (k=1)$ $25.92\ kg\ m^{-3}\ (k=2)$ $26.83\ kg\ m^{-3}\ (k=3)$ $27.18\ kg\ m^{-3}\ (k=4)$ $27.39\ kg\ m^{-3}\ (k=5)$ $27.77\ kg\ m^{-3}\ (k=6)$
$\sum_{i=1}^{k} H_k$	Rest depth at base of layer k	$135\ m\ (k=1)$ $320\ m\ (k=2)$ $550\ m\ (k=3)$ $800\ m\ (k=4)$ $1050\ m\ (k=5)$ $6500\ m\ (k=6)$

2.2 Model Response to Large-Scale Wind Forcing

Model-data comparisons using a variety of domain configurations and resolutions demonstrate that the NLOM produces realistic results for the Pacific Ocean north of $20.0^{o} S$. [*Donohue et al.*, 1994; *Hogan et al.*, 1992; *Hurlburt et al.*, 1992, 1996; *Jacobs et al.*, 1994, 1996; *Kindle and Phoebus*, 1995; *Melsom et al.*, 1995, 1998; *Metzger et al.*, 1992, 1994; *Metzger and Hurlburt*, 1996; *Mitchell et al.*, 1996; *Mitchum*, 1995] Of particular note is comparison by *Melsom et al.* [1998] of sea surface height correlations at Sitka, Alaska. These show that good results can be obtained even in areas where isopycnal outcropping is expected.

isopycnal outcropping is expected.

The model reproduces all the major circulation features in and around the Gulf of Alaska. (Figure 1) The zonal subarctic current is evident at about $45^{o} N$ latitude. Its

terminus lies at approximately $150°W$ longitude, where meridional coherence disintegrates into an alternating blend of powerful cyclonic and anticyclonic eddies. Along the eastern continental margin, the Alaska Current ambles northwestward until it curves around the southern coast of Alaska and accelerates west of Kodiak Island, becoming the Alaskan Stream. The timing and position of recirculation filaments connecting the Alaskan Stream to the subarctic current vary according to local wind stress curl [*Thomson*, 1972]. The interior of the Alaskan Gyre, which is defined by these boundaries, exhibits intense mesoscale activity in agreement with *Cummins and Freeland* [1993].

3. EXPERIMENT METHODOLOGY

The experiment consists of four major steps. First, the analytical circulation equation is derived from the model equations of motion. This equation expresses vorticity balances as derived quantities of variables in the original equations of motion. Second, it is discretized in space and time in order to form an easily solvable algebraic equation. Third, gridded fields of model data from a single layer are used to calculate a value for each term in the algebraic equation. This is done for each data record, enabling time series of each term to be made. Finally, the scalar and field time series of the original and derived physical quantities are displayed visually in ways conducive to revealing the physics underlying interannual variability of vorticity in the Gulf of Alaska.

The horizontal domain of the experiment is the region defined by a western boundary situated at $205^o\,E$, a southern boundary at $50^o\,N$, and the adjoining British Columbian and Alaskan coasts. (Figure 1) Quantitative evaluation of the spatial and temporal variability of vorticity along all potential boundaries (not shown here) indicates that these are an optimal compromise between the need to minimize stochastic influences along the periphery of the Gulf of Alaska and the desire to keep the domain as large as possible. Undesirable influences include the massive vorticity signature associated with the terminus of the Pacific Current and that associated with flow through the Unimak Pass.

A model layer within this domain can exchange vorticity through its western and terminus of the Pacific Current and that associated with flow through the Unimak Pass.

A model layer within this domain can exchange vorticity through its western and southern boundaries and its upper and lower layer interfaces. (Figure 2a)

wind stress curl

advection through
western boundary

advection through
southern boundary

diapycnal mixing
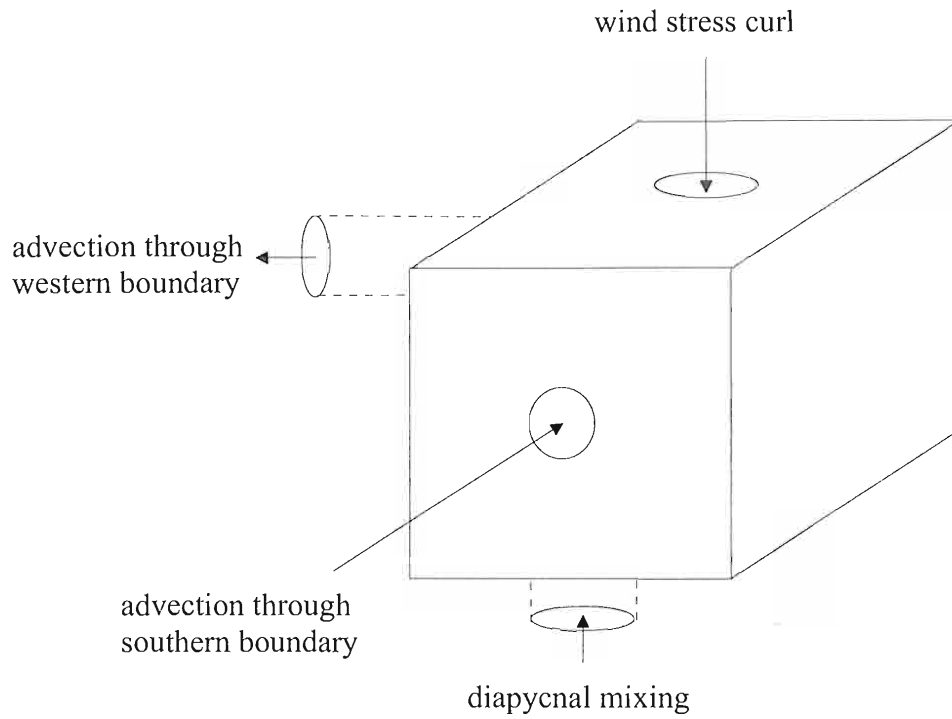
FIGURE 2a: Diagram of vorticity pathways into and out of the study domain.

LAYER 1

u1, v1, h1

LAYER 2

u2, v2, h2

INTEGRATION OF
LAYERS 1 & 2

$h12 = h1 + h2$

$u12 = \dfrac{u1*h1 + u2*h2}{h12}$

$v12 = \dfrac{v1*h1 + v2*h2}{h12}$
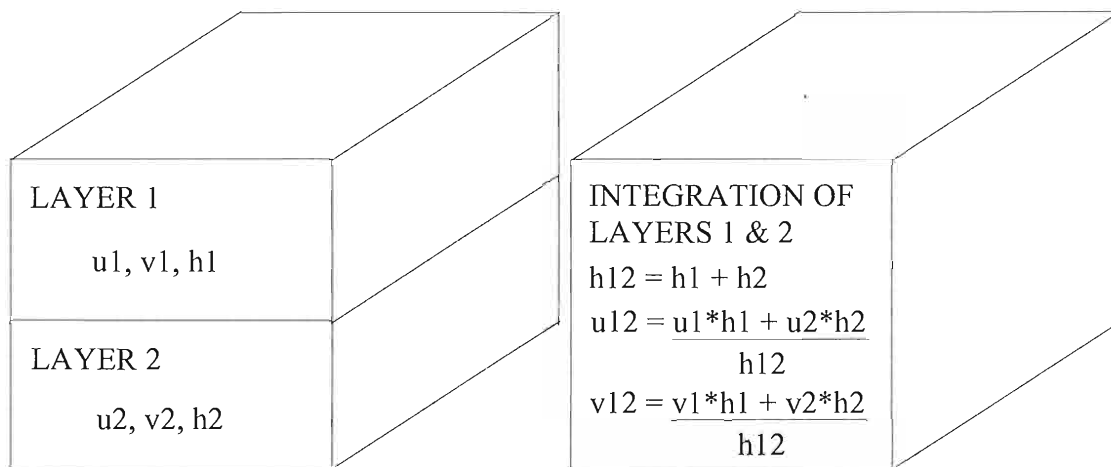
FIGURE 2b: Diagram of construction of integrated layers.

The vorticity imparted by the wind stress curl through the air/sea interface into the upper layer is particularly important. In addition, some vorticity is lost to diffusion within the layer, but this will be shown later to be negligible.

The circulation equation is used to quantify the influence of these vorticity-transport pathways. This equation is derived directly from the model equations of motion.

$$C(t) - C(0) = \int_0^t \int_{SW}^{NW} u(\zeta + f)dydt + \int_0^t \int_{SW}^{SE} v(\zeta + f)dxdt + \int_0^t \oint_D (\hat{k} \bullet \nabla \times \frac{\bar{\tau}_W}{\rho_0 h})dAdt +$$

$$A_H \int_0^t \oint_D (\nabla^2 \zeta)dAdt + R, \text{ where } R \text{ is a residual representing the curl of}$$

the interfacial terms

Its first term is a circulation anomaly relative to the first data record. The second through fifth terms are the contributions to the circulation from advection of vorticity across the western and southern boundaries, applied wind stress curl, and diffusion, respectively. The sixth term, R, quantifies the change in circulation associated with vorticity input to a layer across a horizontal interface due to hydromixing. Physically, R represents three processes: stress associated with the curl of interfacial friction, stress due to friction associated with entrainment, and vertical advection of vorticity by hydromixing. Because all of the other terms are to be computed, the residual can be calculated for each data record by subtracting the boundary, curl, and diffusion terms from the circulation anomaly. Evaluating them with this technique obviates the need to keep the interfacial terms in the derivation of the circulation equation, which can be found in Appendix B.

The equation is valid for any single layer of arbitrary rest thickness, so long as its upper interface is the air/sea boundary. This property is exploited to examine the baroclinicity of vorticity balances within the domain. Time series of the circulation equation terms are calculated for three layers: layer 1, an integration of layers 1 and 2, and an integration of layers 1, 2, and 3. An integrated layer h field is comprised of an element by element sum of the h fields of its constituent layers. Integrated-layer u and v fields are calculated by dividing the sum of the transports of their constituent layers by the sum of their thicknesses. (Figure 2b) Transports for a given layer are computed with an element by element multiplication of velocity and layer thickness. The integrated layer u, v, and h fields are then used to calculate derived quantities which are average values over the depth of the integrated layer h field. However, the same wind stress fields are used in the calculation of the wind stress curl term regardless of the choice of layer depth.

Construction of time series of the circulation equation terms from a layer's u, v, and h fields is a multi-step process involving the differencing and integration of gridded fields. All derivatives are first order centered differences. Line and surface integrals use segments and rhomboidal areas proportioned for the poleward decrease of zonal grid spacing. First, the space integrals inside the second through fifth terms are evaluated for each data record. Next, the circulation, equal to the surface integral of vorticity over the domain, is calculated for each data record. The mean of this series is computed, and the series examined to find where it first crosses the mean. The preceding portion is truncated. Taking this new circulation time series to be $C(t)$, with its first record $C(0)$ being equal to the mean, sets the first term in the circulation equation, $C(t)-C(0)$, to a true

circulation anomaly.

The time series of space integrals in terms two through five are truncated in an identical manner, maintaining the simultaneity of all series. The evaluation of these terms is then completed by integrating in time from the first data record, where the circulation anomaly is zero. This is done by successively adding the previous data record to the product of the new data record and the temporal separation. $[\sum a_{j-1} + a_j * \Delta t]$ Next, all time series are filtered with a 14-month running average to attenuate subannual variations. Various visualizations and statistical comparisons of these time series and the derived and native quantities with which they are constructed should allow evaluation of the physics underlying interannual vorticity variability in the Gulf of Alaska.

4. RESULTS

4.1 Synopsis

The interannual variability of vorticity balances in the Gulf of Alaska is largely due to atmospheric and oceanic teleconnections originating with the El Niño-Southern Oscillation. The Aleutian Low weakens during the early phase of El Niño events [*Emery and Hamilton,* 1985; *Putman,* 1998], reducing the amount of vorticity injected into the upper ocean by the wind stress curl. El Niño events also excite poleward-traveling downwelling coastal Kelvin waves on the eastern continental margin of the equatorial Pacific Ocean. These waves strengthen the Alaska Current at the peak of its annual cycle, triggering baroclinic instabilities which result in the formation of a coast-wide train of anticyclonic eddies [*Melsom et al.,* 1995; 1998]. The more southerly of these eddies tend to propagate to the southwest, carrying negative vorticity out of the Gulf of Alaska. This net gain of vorticity is inversely correlated with and serves to balance the nearly contemporaneous reduction of vorticity input by the wind stress curl. Due to the baroclinic nature of both the eddies and the influence of the wind stress curl, the effect is largely confined to the upper ocean.

4.2 Atmospheric Forcing

4.2 Atmospheric Forcing

The Aleutian Low is the dominant atmospheric circulation feature in the northeast Pacific Ocean, and is the driving force behind the cyclonic mean flow regime in the Gulf

of Alaska. *Emery and Hamilton* [1985] suggest that weak winter atmospheric circulation

in the North Pacific often precedes major El Niño events and is followed by a rapid

restrengthening of the circulation pattern. This sequence is verified in observations

analyzed by *Putman* [1998]. The curl of wind stress divided by upper layer thickness is a

measure of how much vorticity is being injected into the upper layer at a given location.

Its surface integral is a measure of injected vorticity over the domain. A time series of

this quantity for the Gulf of Alaska reveals a pattern closely matching the progression

espoused in *Emery and Hamilton* [1985]. (Figure 3) Relative lows in 1982-83, 1985-86,

and 1993 are all followed by strong relative highs. All occur during El Niño events as

defined by the JMA Index. (Figure 4)

4.3 Coastal Kelvin Waves

Tropical Pacific cyclones are a major source of the equatorial Kelvin waves

associated with El Niño events [*Kindle and Phoebus*, 1995]. An eastward moving

equatorial Kelvin wave reflects off the eastern boundary in the form of a westward-

traveling Rossby wave and two poleward traveling coastal Kelvin waves [*Clarke*, 1983].

Meyers, et al. [1998], extending work by *Chelton and Davis* [1982] and *Enfield and Allen*

[1980], use coastal sea level data along the northeast Pacific Ocean to verify that coastal

Kelvin waves propagate from the equator to the northern Gulf of Alaska. Recent

modeling studies by *Melsom et al.* [1995, 1998] show that El Niño-induced coastal

Kelvin waves can alter circulation in the Gulf of Alaska by destabilizing the Alaska

Kelvin waves can alter circulation in the Gulf of Alaska by destabilizing the Alaska

Current, spawning coast-wide trains of long-lived anticyclonic eddies.
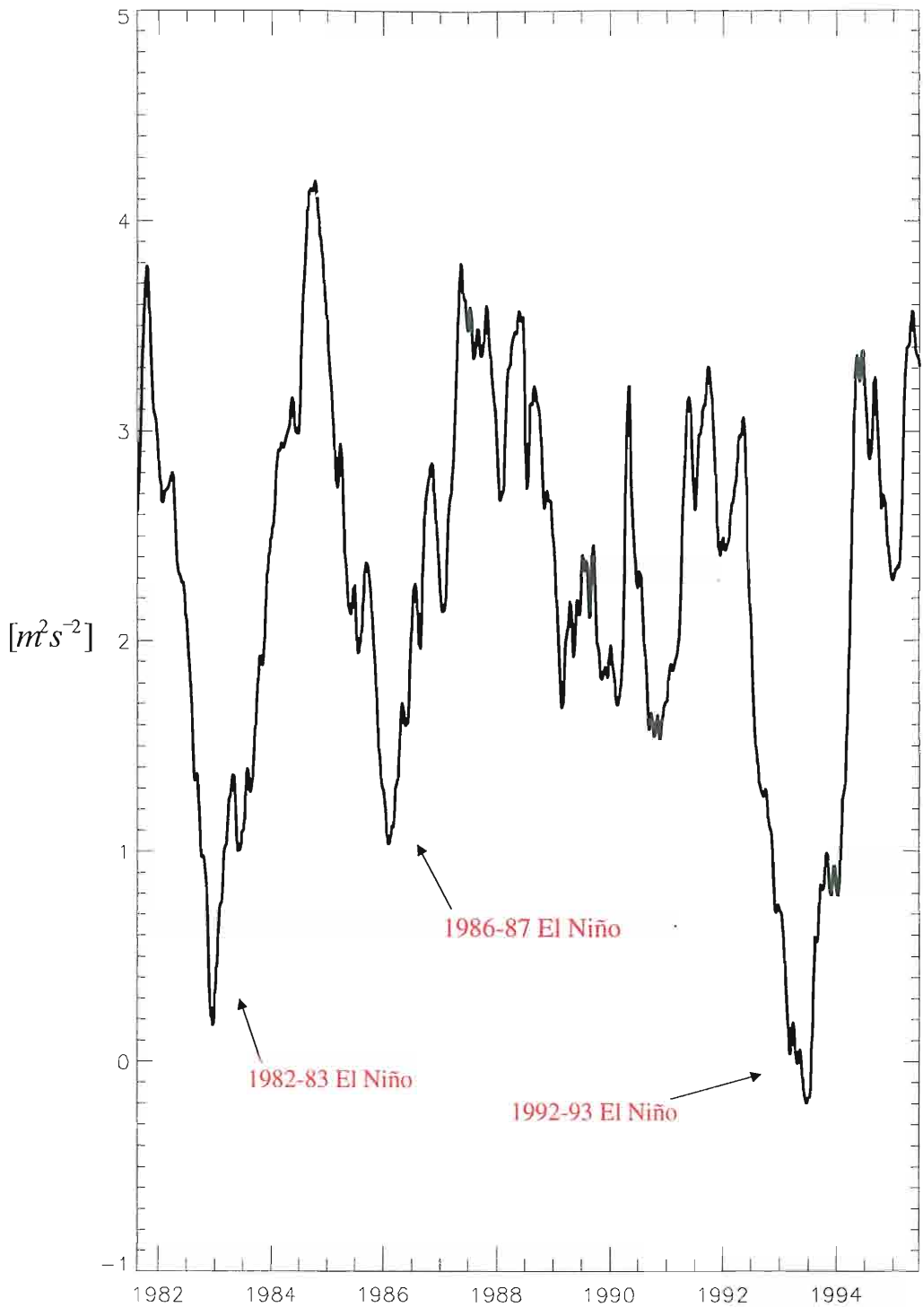
FIGURE 3: Vorticity imparted to the upper layer by the wind stress curl from late 1981 to 1995. Smoothed with a 14-month running average.
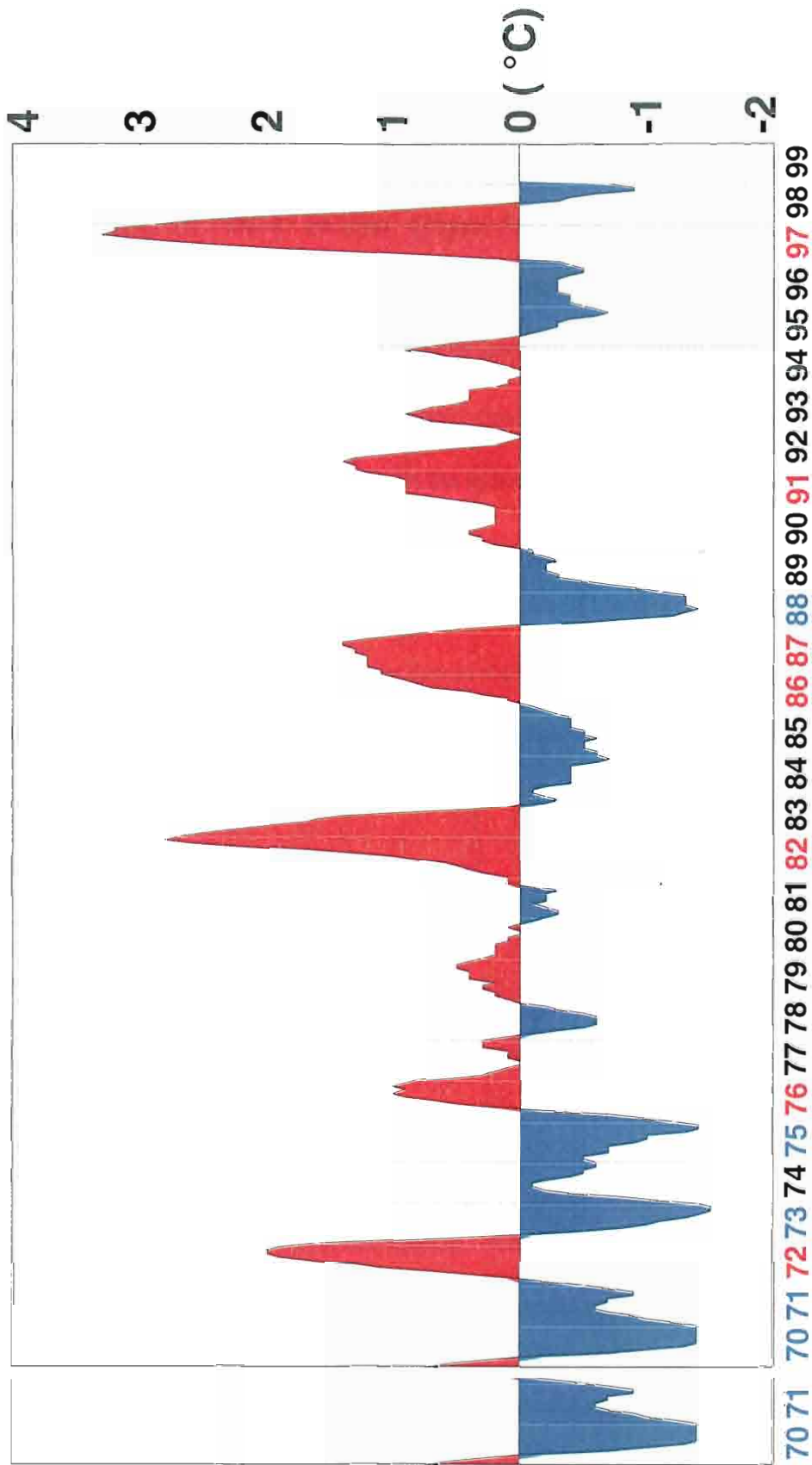
FIGURE 4: JMA Index (Courtesy of Jiraporn Whalley)

18

In the present study, four of the five greatest maxima in the coastal upper-layer thickness time series at $50°N$ occur during the following El Niño years: 1982-83, 1986-87, 1991-92, and 1994-95. (Figure 5) The fifth occurs during the 1985-86 cold event which precedes the 1986-87 El Niño. (Figure 4) The role of these events in internannual variability is best illuminated by removal of the annual climatology. (Figure 6) All of the maxima occur on or near the peak of the annual cycle, and all are preceded by a characteristic sharp increase in the anomaly time series. These sharp increases do not appear to be correlated with changes in the space-integrated wind stress curl, which is increasing during the 1985-86 and 1986-87 upper layer thickness maxima, and decreasing during the 1982-83, 1991-92, and 1994-95 maxima. This disparity precludes the possibility that the maxima are solely due to increased Ekman pumping from an intensified atmospheric circulation pattern. The sharp increases in upper layer thickness must therefore be due at least in part to tropically-forced downwelling coastal Kelvin waves.

Downwelling coastal Kelvin waves can occur during cold periods [Dr. J.J. O'Brien, personal communication]. Both fully extant cold events in the model record, 1984-85 and 1988-89, contain a downwelling coastal Kelvin wave. However, only the former event was sustained during the peak of the annual cycle, allowing for destabilization of the Alaska Current. (Figure 6)

Wind stress curls, while decreasing, were still quite strong preceding the 1986-87 and 1991-92 thickness anomaly maxima. This model result tends to corroborate *Meyers, et al.* [1998] suspicion that sea level variation during the 1986-87 and 1991-92 events
was a combination of remote and local wind forcing.
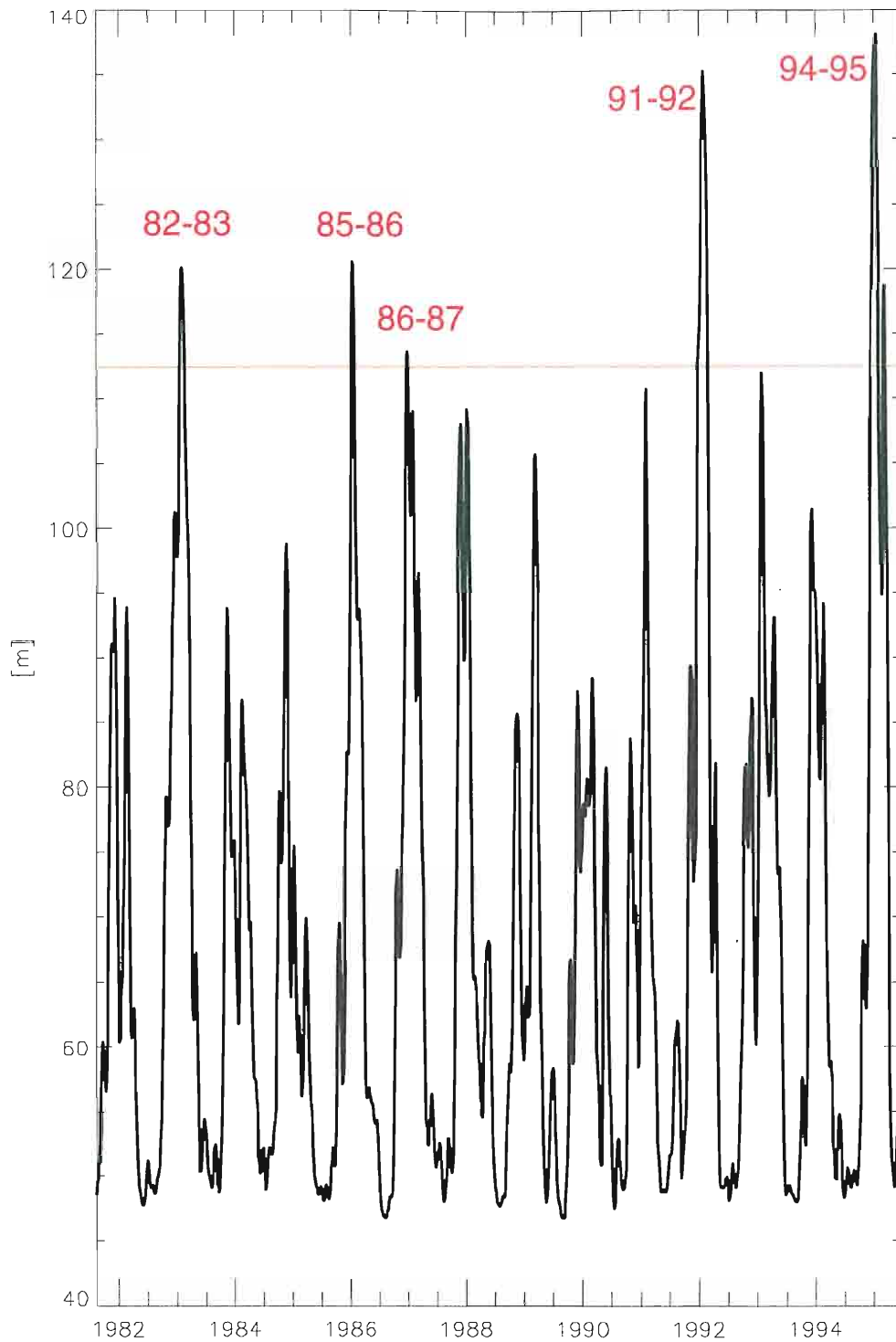
FIGURE 5: Coastal upper layer thickness at 50N from late 1981 to 1995. Smoothed with several Hanning passes. The arbitrary red bar is set to 112*m*.

FIGURE 5: Coastal upper layer thickness at 50N from late 1981 to 1995. Smoothed with several Hanning passes. The arbitrary red bar is set to 112*m*.
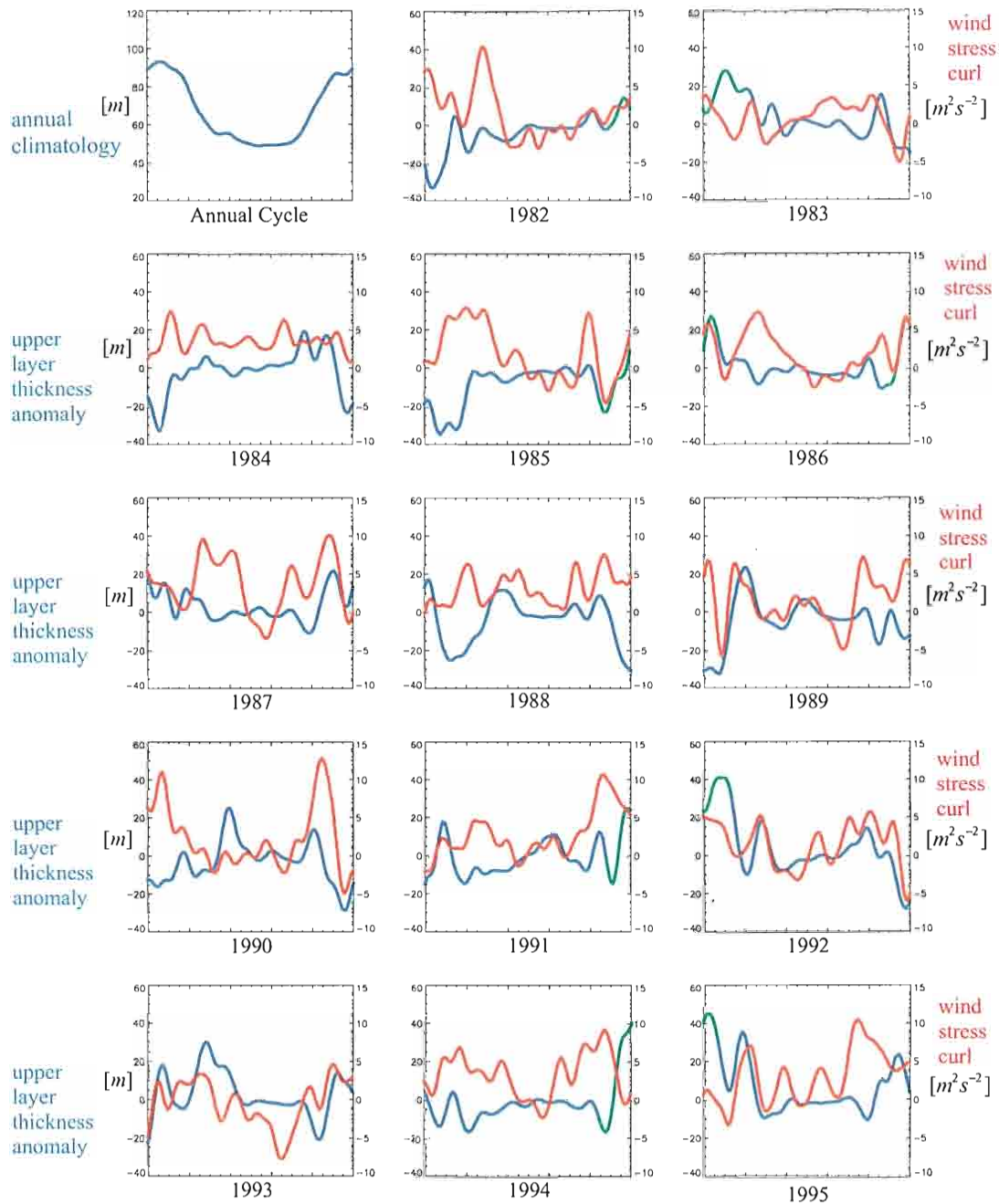
FIGURE 6: Vorticity gain in the upper layer from the wind stress curl plotted with coastal upper layer thickness anomaly from the climatology at 50N from 1982 to 1995. The first segment is the upper layer thickness annual climatology. Coastal Kelvin wave events associated with destabilization of the Alaska Current are shown in green. All are at 50N from 1982 to 1995. The first segment is the upper layer thickness annual climatology. Coastal Kelvin wave events associated with destabilization of the Alaska Current are shown in green. All are smoothed with several Hanning filters.

21

4.4 Eddy Train Genesis and Fate

Coast-wide eddy trains whose diameter and spacing are consistent with generation by baroclinic instability processes have been modeled by *Melsom et al.* [1995, 1998], and observed by *Thomson and Gower* [1998]. In this experiment, eddy activity is revealed in the model upper layer thickness throughout the record. Eddy trains consisting of at least small and short-lived eddies appear in every year except those following the 1988-89 La Niña. This model result strongly supports *Thomson and Gower's* [1998] hypothesis of the existence of an annual cycle of eddy generation. The absence of eddy trains following the 1988-89 La Niña is highly suggestive of a link between the annual cycle and the El Niño-Southern Oscillation, and is consistent with altimetry observations by *Meyers and Basu* [1998]. Whether intraseasonal coastal Kelvin waves not related to El Niño or perturbations in the local wind stress field drive the annual cycle is unknown.

Coast-wide trains of robust mesoscale eddies appear five times in the model record: 1983, 1986, 1987, 1992, and 1995. The number and spacing of the 1995 eddy train shows close agreement to the contemporaneous composite thermal image discussed in *Thomson and Gower* [1998]. (Figure 7) The eddies observed in these five years are sharply differentiated from those of other years by their size and longevity. They can exceed 200 *km* diameter and last more than a year, whereas the smaller eddies never exceed 80 *km* and rarely last more than two months. All of the large-eddy trains appear during or near El Niño years as defined by the JMA Index, and all three El Niño events in the model record contain at least one large-eddy train. Examination of the $50°N$ coastal

~~upper layer thickness anomaly time series reveals the most incriminating observation: all~~

the model record contain at least one large-eddy train. Examination of the $50°N$ coastal upper layer thickness anomaly time series reveals the most incriminating observation: all of the large-eddy trains appear immediately following relative maxima which have been

22
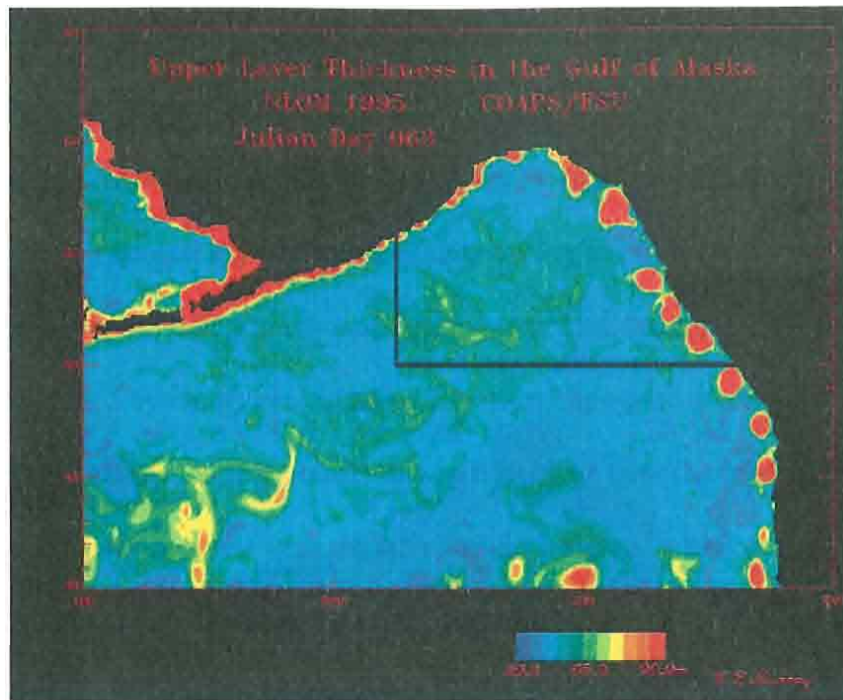
FIGURE 7a: Contours of model upper layer thickness in the Gulf of Alaska on 4 March 1995. The black lines demarcate the southern and western boundaries of the study region.
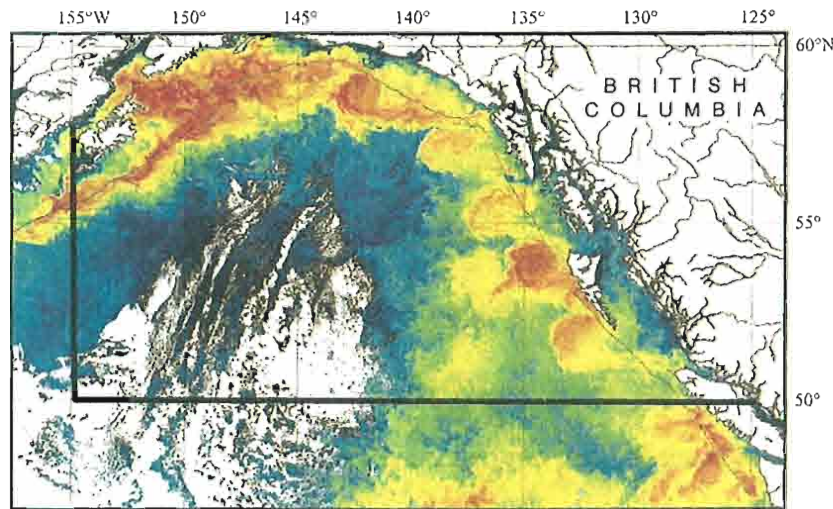
FIGURE 7b: Composite thermal image of the Gulf of Alaska from AVHRR data for March 1, 2, 3, and 10. The black lines demarcate the southern and western boundaries of the study region. From *Thomson and Gower* [1998].
AVHRR data for March 1, 2, 3, and 10. The black lines demarcate the southern and western boundaries of the study region. From *Thomson and Gower* [1998].

shown in the previous section to be linked with tropically forced coastal Kelvin waves. (Figure 6)

Geostrophic increases in the mean flow of the Alaska Current caused by powerful tropically-forced coastal Kelvin waves excited during El Niño events are therefore the critical component of a large-eddy train genesis event. Contemporaneous increases in the mean flow caused by wind stress induced Ekman pumping no more than enhance the size of an event. However, local reversals in wind stress, as hypothesized in *Thomson and Gower* [1998], may compete with the later Kelvin waves of a packet as the source of perturbation necessary to induce baroclinic instability.

Size and latitude of eddy origination in part determine fate. Small eddies are either quickly reabsorbed into the boundary current or tend to dissipate within two months. Large eddies that form near the head of the gulf are inevitably drawn into the Alaskan Stream. Those that form farther south along the coast tend to propagate to the southwest. Some of these appear to be arrested in the center of the gyre while others halt upon reaching the Pacific Current front. Those that reach the front have carried negative vorticity to the periphery of the Gulf of Alaska.

Three types of eddy train generation patterns appear to be present in the model record. No eddy trains appear during La Niñas. During neutral phases, coast-wide trains of small, short-lived eddies emerge, usually around the peak of the annual cycle of the Alaska Current. These weaker events may be caused by intraseasonal coastal Kelvin waves or wind stress reversals. Coast-wide trains of large, long-lived eddies occur only during El Niños and are always preceded by tropically forced coastal Kelvin waves.
waves or wind stress reversals. Coast-wide trains of large, long-lived eddies occur only during El Niños and are always preceded by tropically forced coastal Kelvin waves.

Only these latter eddies have the size and longevity necessary to serve as conduits for consequential negative vorticity advection out of the Gulf of Alaska.

4.5 Vorticity Balances

4.5.1 Interannual Variability

Interannual variability in the circulation of the Gulf of Alaska, as measured by the surface integral of vorticity, is miniscule relative to its mean. (Figure 8) Annual inputs and outputs of vorticity through the available pathways, advection through the western and southern boundaries, diffusion, applied wind stress curl, and diapycnal mixing, are not small relative to the mean. Interannual variations in these sources and sinks balance to maintain the constancy of the circulation.

The wind stress curl is the largest vorticity source of the upper layer. Although weaker in magnitude, interannual variations in the vorticity advection through the southern boundary tend to balance interannual variations in the wind stress curl. (Figure 9) The relationship is quantified by a linear correlation coefficient of -0.62. Most of the interannual variability in the vorticity added by wind stress curl is associated with the Southern Oscillation. (Section 4.2) The interannual variability of vorticity advection across the southern boundary is largely caused by the passage of anticyclonic eddies. All of the large relative highs in the southern boundary time series are associated with the passage of a single eddy.

A Hovmüller diagram of the upper layer thickness proves this by revealing the time

A Hovmüller diagram of the upper layer thickness proves this by revealing the time and longitude of eddy transits across the boundary. (Figure 10) Positive eddy thickness signature indicates that they are anticyclonic, and therefore embody negative vorticity.

25
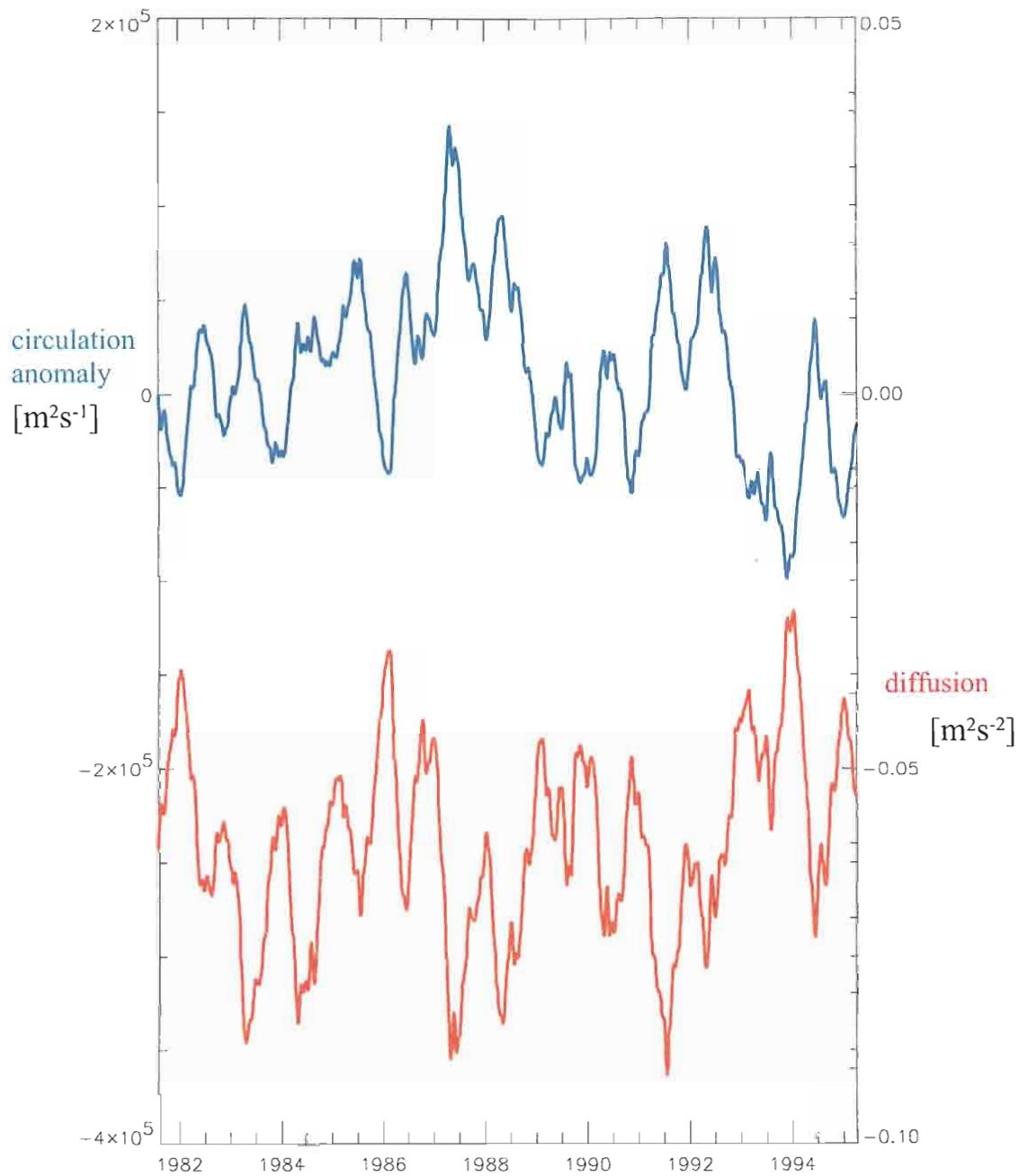
FIGURE 8: Circulation anomaly from the mean of 2.22 x 10⁸ m²s⁻¹ plotted with vorticity loss from diffusion from late 1981 to 1995. Smoothed with a 14-month running average.

Smoothed with a 14-month running average.
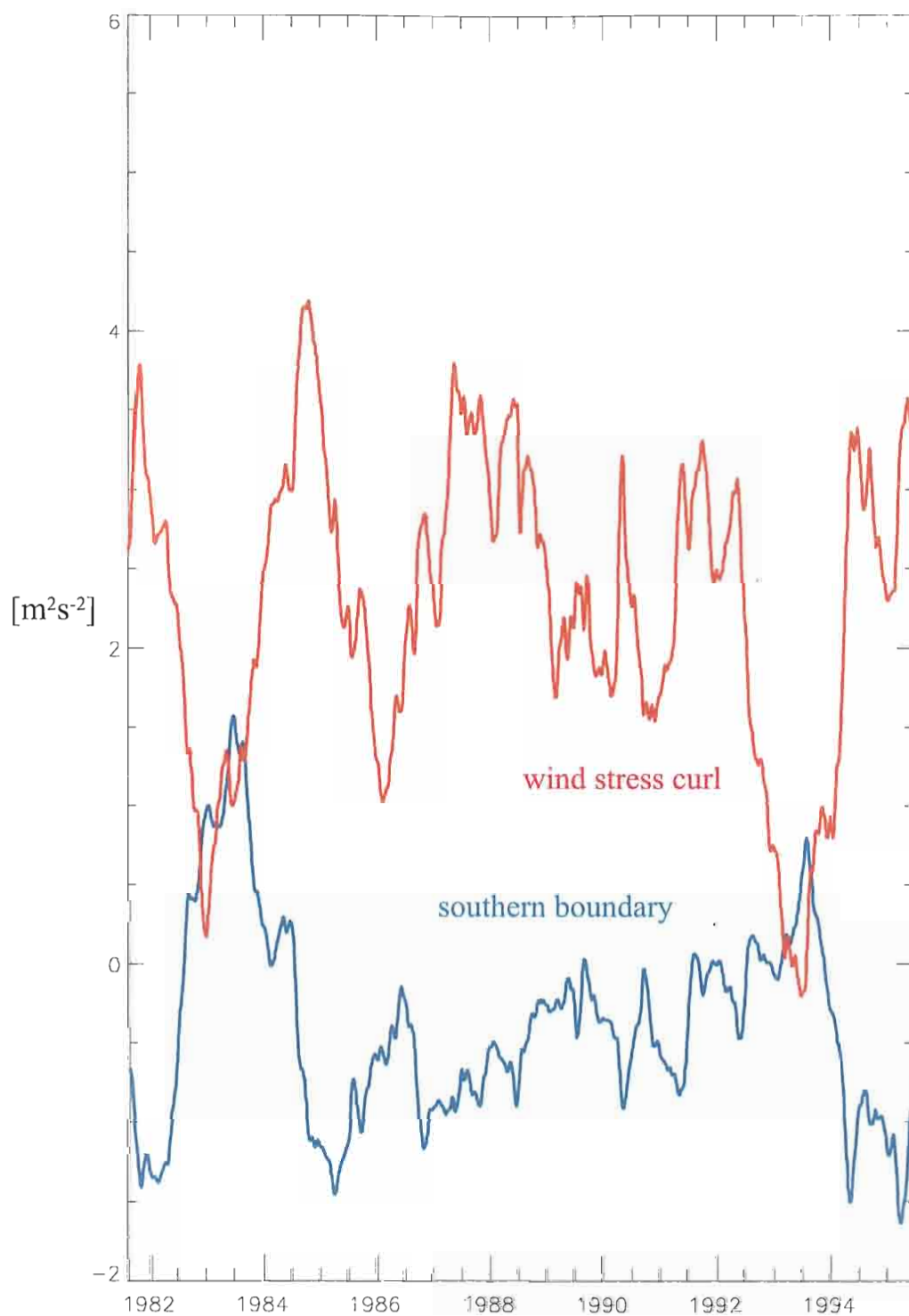
FIGURE 9: Vorticity advection across the southern boundary at 50N plotted with the vorticity gain in the upper layer from the wind stress

FIGURE 9: Vorticity advection across the southern boundary at 50N plotted with the vorticity gain in the upper layer from the wind stress curl. Smoothed with a 14-month running average.
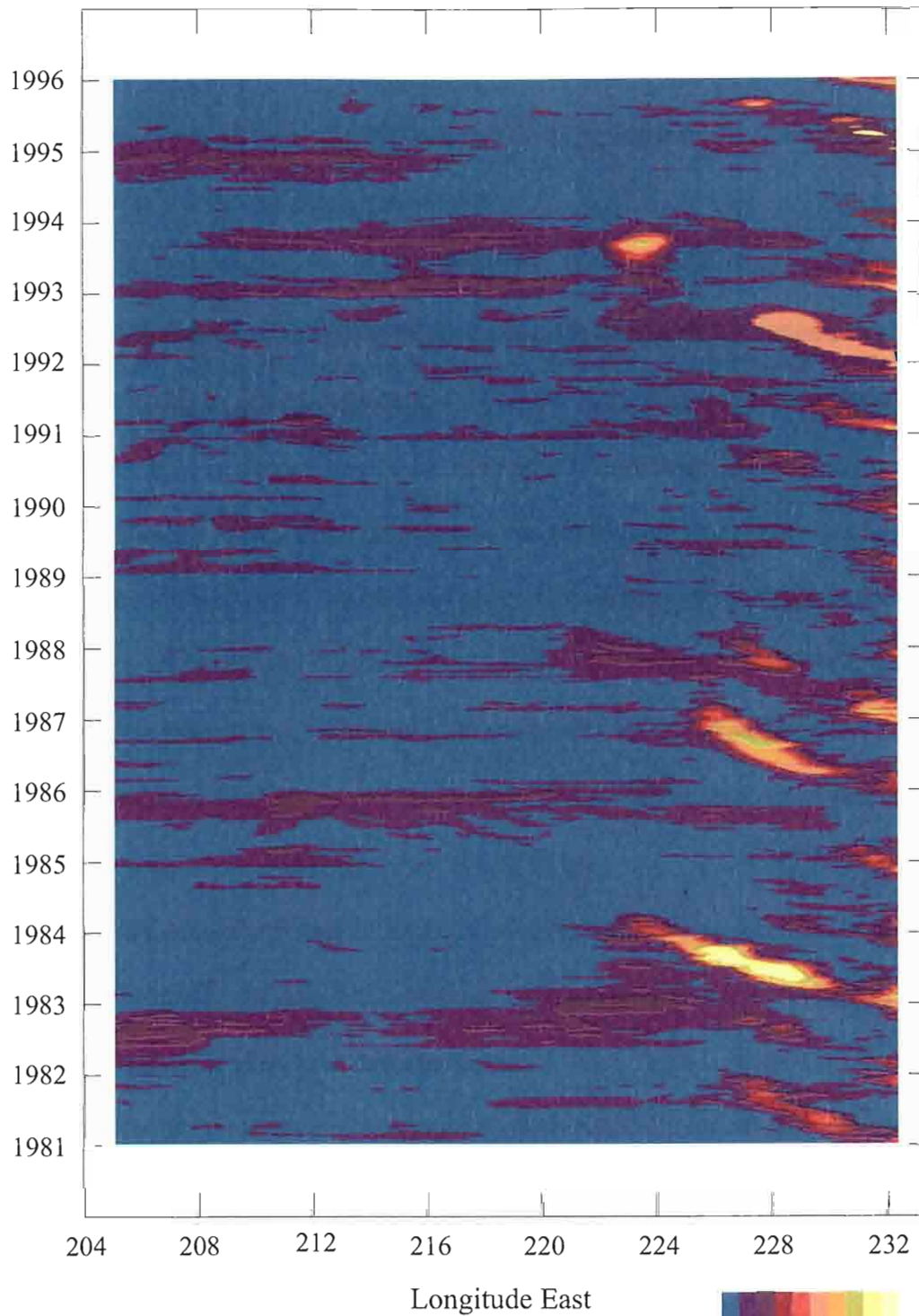
27

FIGURE 10: Hovmuller diagram of upper layer
thickness in meters along the southern boundary

FIGURE 10: Hovmuller diagram of upper layer
thickness in meters along the southern boundary
at 50N.

45.0   95.0   145.0

45.0   95.0   145.0
            meters

28
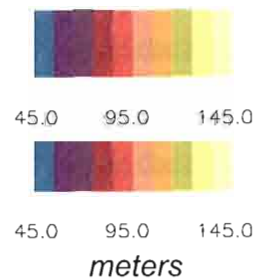
The zonal direction of propagation is revealed to be westward by the negative slope of the layer thickness signature of eddies near the coast. However, this plot contains no information on the meridional direction of propagation; animations of the upper layer thickness reveal it to be uniformly southward.

Vorticity advection across the western boundary is the primary sink of the upper layer. (Figure 11a) The predominant physical mechanism is the continual westward advection of positive vorticity by the Alaskan Stream. (Figure 11b) A strong annual signal is evident, presumably corresponding to the strength of the Alaskan Stream and the annual cycle of the Aleutian Low. The high negative correlation ($r = -0.81$) between the western boundary term and the sum of the curl and southern boundary terms suggests that interannual variation of vorticity advection through the western boundary is driven by variability in the latter terms. Therefore, it appears that the Alaskan Stream serves as a 'vorticity overflow valve' responsive on interannual time scales and compensating for imbalances wrought by the driving terms. (Figure 11a)

Diffusion is a secondary vorticity sink. It is highly negatively correlated with circulation. (Figure 8) Its role in the vorticity balance is minor due to its being two orders of magnitude smaller than the other terms.

The last term, R, is always positive in the Gulf of Alaska due to widespread ispycnal outcropping and thin layers. It is due to hydromixing, where mass and momentum from the underlying layer are added to h grid points whose h values fall below a predetermined level. Because this is done on a grid point by grid point basis, at the time the mass is added, it serves to increase h only at that grid point. This is analogous to adding mass level. Because this is done on a grid point by grid point basis, at the time the mass is added, it serves to increase h only at that grid point. This is analogous to adding mass
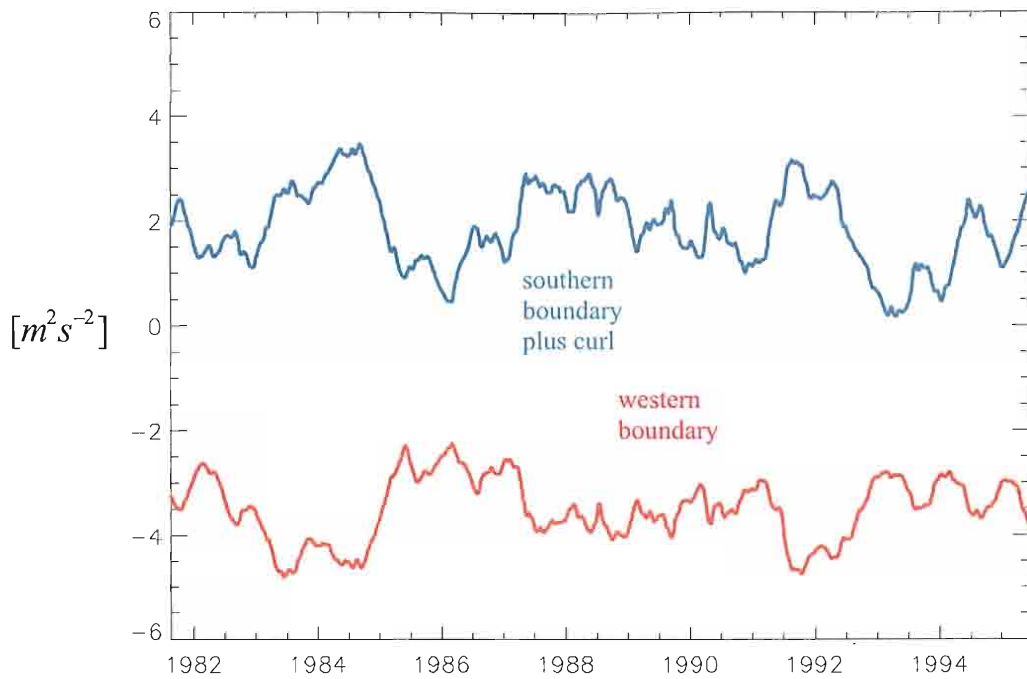
FIGURE11a: Vorticity advection across the western boundary plotted with the sum of the southern boundary and curl terms. Smoothed with a 14-month running average.
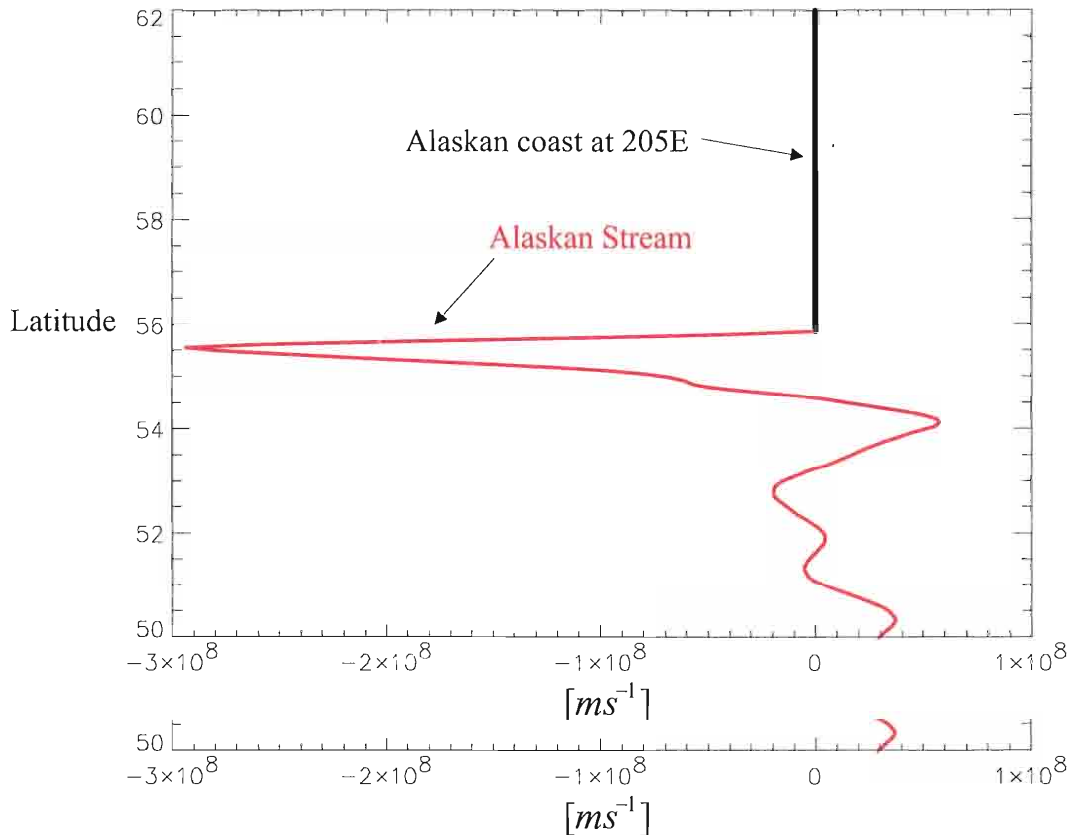
FIGURE 11b: Time integral over the data record of vorticity advection across the western boundary at each latitude.

through the bottom of a vortex tube with a fixed diameter. The addition of mass can only stretch the tube, increasing its vorticity.

The shallow level of the upper layer in much of the domain of this experiment ensures substantial hydromixing. This manifests as a vorticity source in magnitude second only to that of the wind stress curl. However, the variance of R is a fifth of the variance of the wind stress curl, and a half of that of the boundary terms. This highlights its relative lack of importance in an examination of the interannual variability of balancing terms.

Moreover, R is highly negatively correlated (r = -0.88) with the wind stress curl. Therefore, most of its interannual variability is driven by interannual variability in the wind stress curl, which is related to the El Niño-Southern Oscillation. The physical basis underlying the correlation can be explained with the use of a vortex tube.

Wind stress curl acting on the top of a vortex tube will impart to it positive vorticity, stretching it. For a vortex tube centered on an h grid point, this is equivalent to increasing h. For a vortex tube with height smaller than the entrainment depth, an increasing h acts to decrease the amount of hydromixing. Therefore, an increase in the wind stress curl will act to decrease R.

The time-integrated terms in the circulation equation represent the cumulative effect on the circulation anomaly in the Gulf of Alaska of vorticity flow through the various pathways. Visual inspection of these terms can best illuminate the relative importance of their variability in the maintenance of the constancy of the circulation. (Figure 12a) This plot displays the cumulative effects of the 1982-83 El Niño on importance of their variability in the maintenance of the constancy of the circulation.

(Figure 12a) This plot displays the cumulative effects of the 1982-83 El Niño on

31

FIGURE 12a: Normalized circulation anomaly and constituent
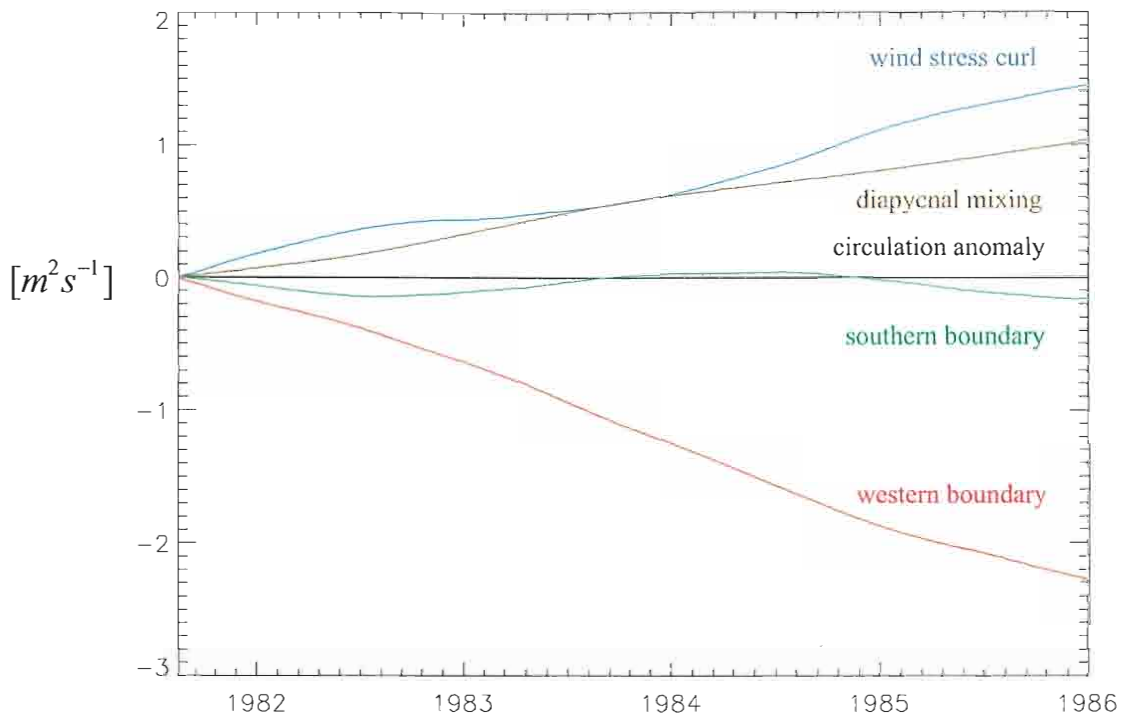time-integrated vorticity terms for layer 1 from late 1982 to 1986.
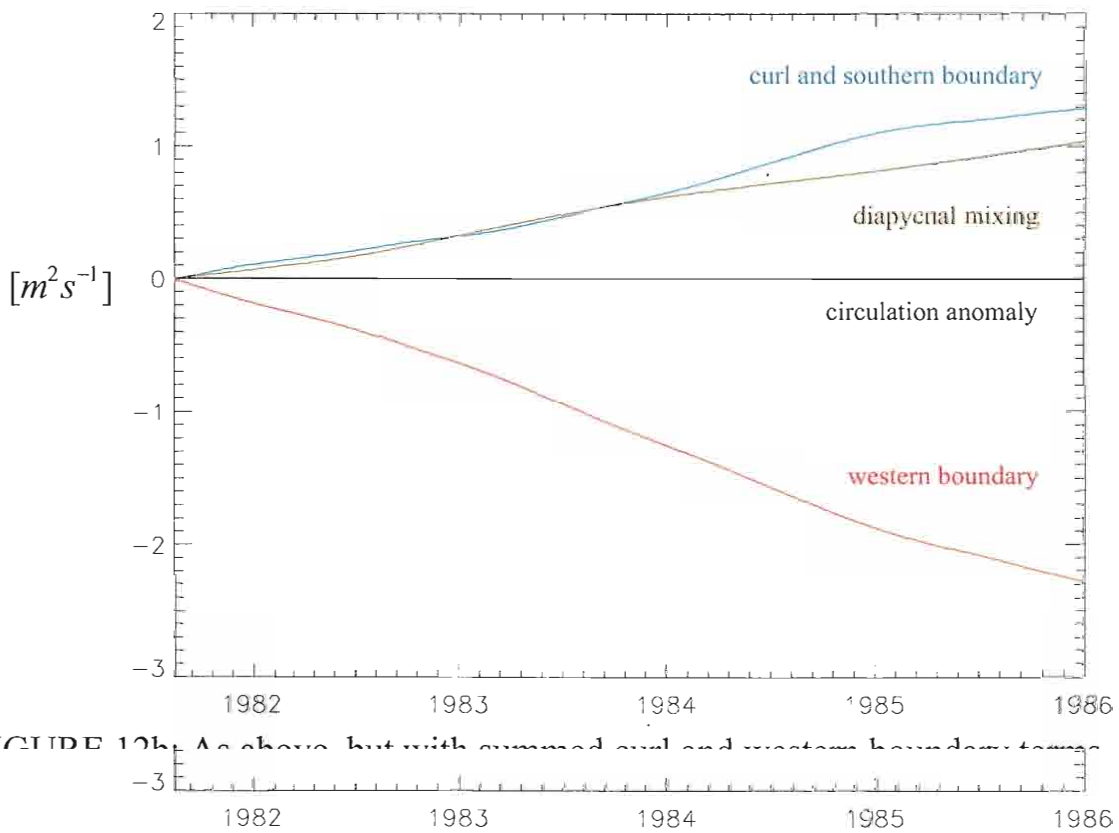
FIGURE 12b: As above, but with summed curl and western boundary terms.

vorticity balances in the Gulf of Alaska. All of the terms have been normalized by the mean of the circulation in order to facilitate comparison with it.

The time-integrated wind stress curl shows the reduction in vorticity input associated with the weakening of the Aleutian Low superimposed upon an essentially linearly increasing trend. The time integrated western boundary term shows the net increase in circulation resulting from the transit of a large eddy spawned during the 1982-83 El Niño superimposed upon an essentially linearly decreasing trend. R is nearly linear, leaving interannual variability in the time-integrated western boundary term to balance variations in the sum of the time-integrated curl and southern boundary terms. (Figure 12b) These time series also reveal that the replenishment time scale of vorticity in the Gulf of Alaska is about two years. The other two El Niños in the model data record display similar patterns.

4.5.2 Baroclinicity

The advection of anticyclonic eddies across the southern boundary and variations of applied wind stress curl are the two driving mechanisms of interannual variability in vorticity balances in the Gulf of Alaska. The anticyclonic eddies and the influence of the wind stress curl are both baroclinic. Analysis of integrated layers comprised of layers one and two, and layers one, two, and three verifies that the interannual vorticity variations associated with them are also baroclinic. The baroclinicity of the circulation is revealed by its substantial decrease in layer 3. (Figure 13) The decay with depth of the influence on interannual variation of both wind stress curl and diapycnal mixing is revealed by the depth dependant decline of their respective variances. The dissolution of influence on interannual variation of both wind stress curl and diapycnal mixing is revealed by the depth dependant decline of their respective variances. The dissolution of these time series leads to an uninteresting input/output balance between the southern and

33
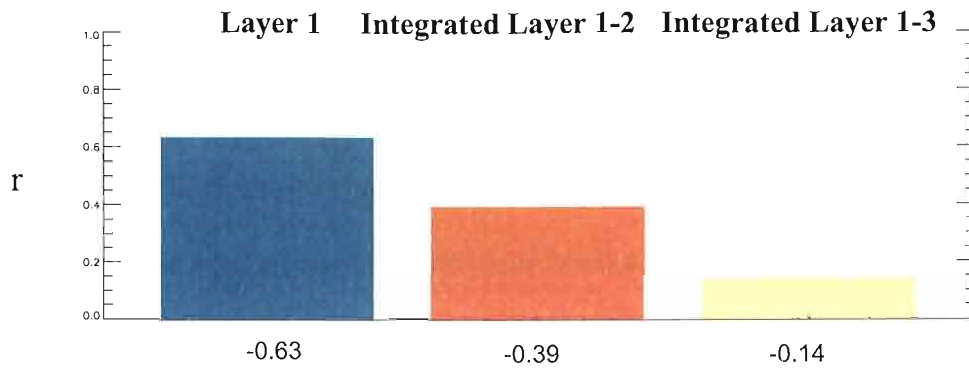
FIGURE 13a: Negative correlation coefficients between the wind stress curl and southern boundary terms for layers 1, 1-2, & 1-3.
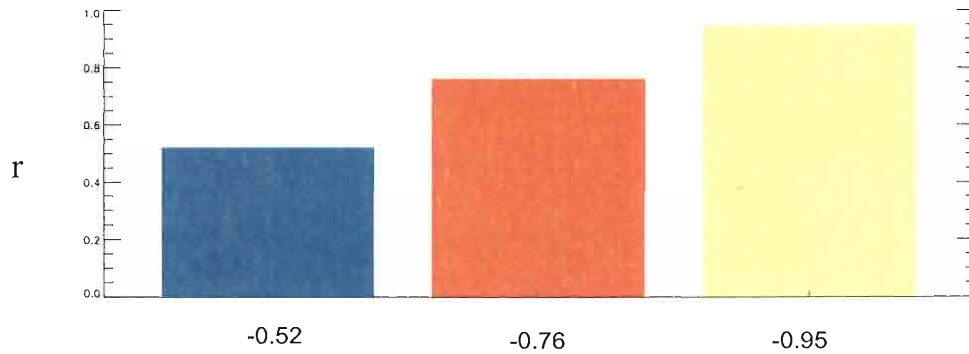
FIGURE 13b: Negative correlation coefficients between the western boundary and southern boundary terms for layers 1, 1-2, & 1-3.
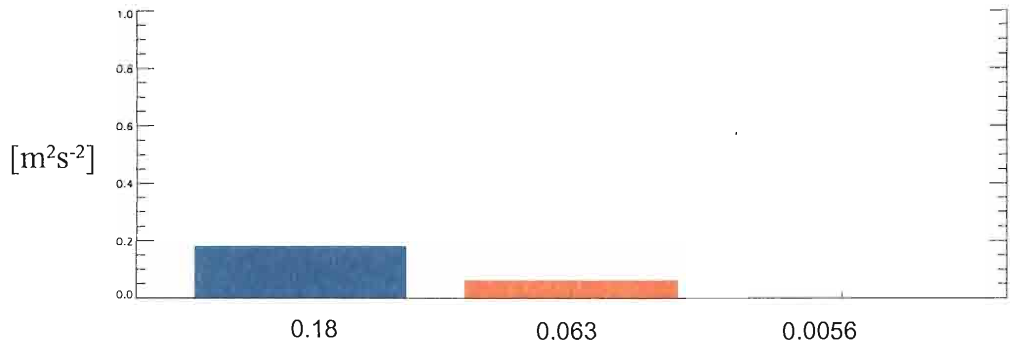
FIGURE 13c: Variances of the interfacial terms for layers 1, 1-2, & 1-3.
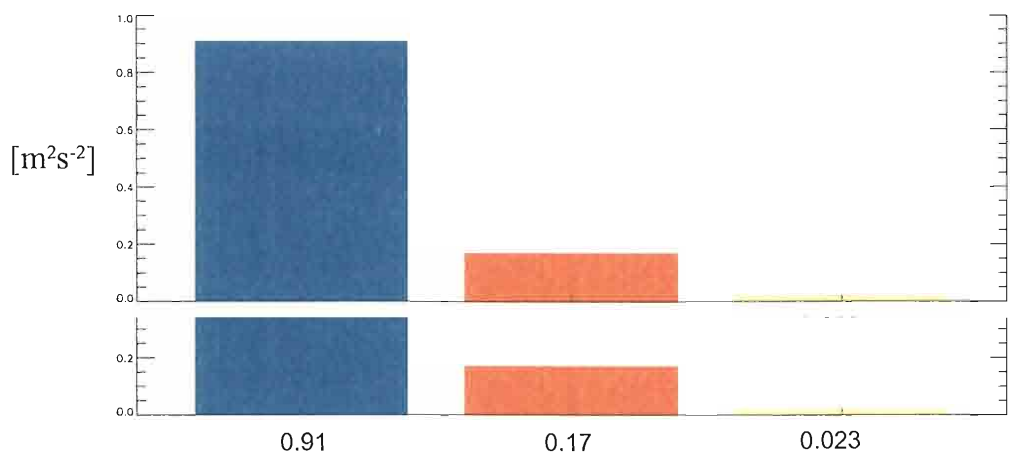
FIGURE 13d: Variances of the wind stress curl for layers 1, 1-2, & 1-3.

western boundary terms. This is shown by the increase with depth of their negative

correlation coefficients, but can be most clearly seen by examination of the time-

integrated series of the thickest integrated layer. (Figure 14) Also, the decline with depth

of the variance of the wind stress curl leads to the breakdown of the interannual variation

balance between it and variation in the southern boundary term. This decomposition is

quantified by the decline of their negative correlation coefficients.
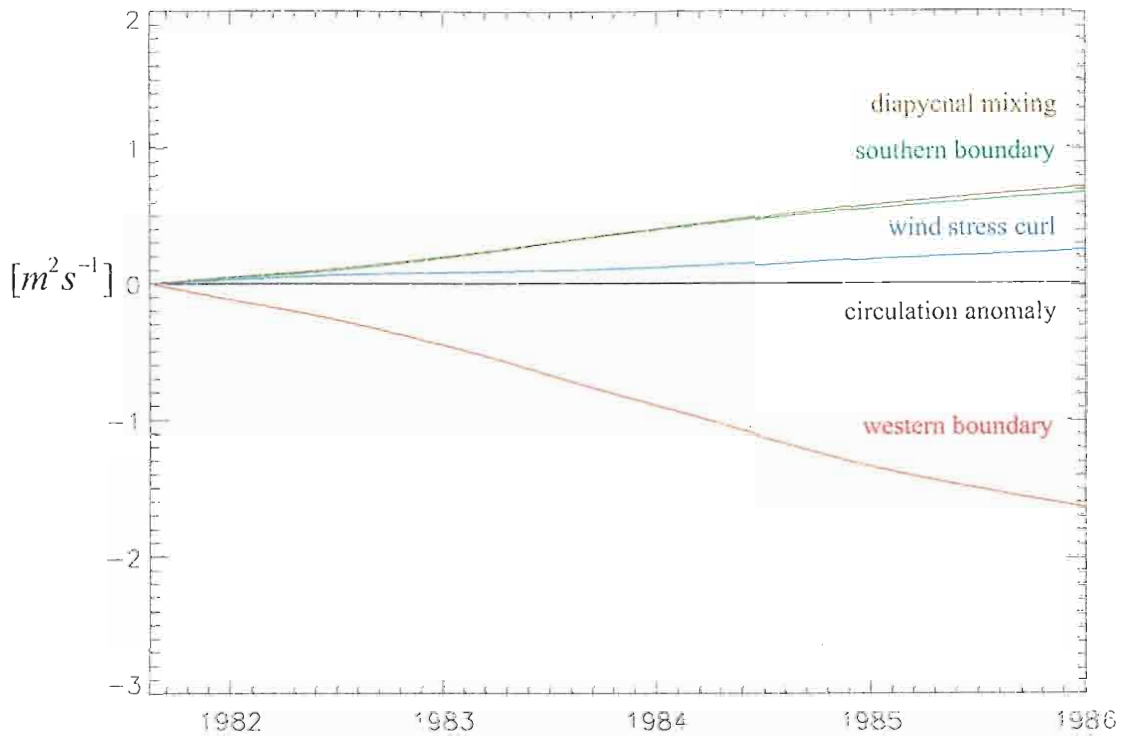
FIGURE 14a: Normalized circulation anomaly and constituent
time-integrated vorticity terms for layer 1 from late 1982 to 1986.
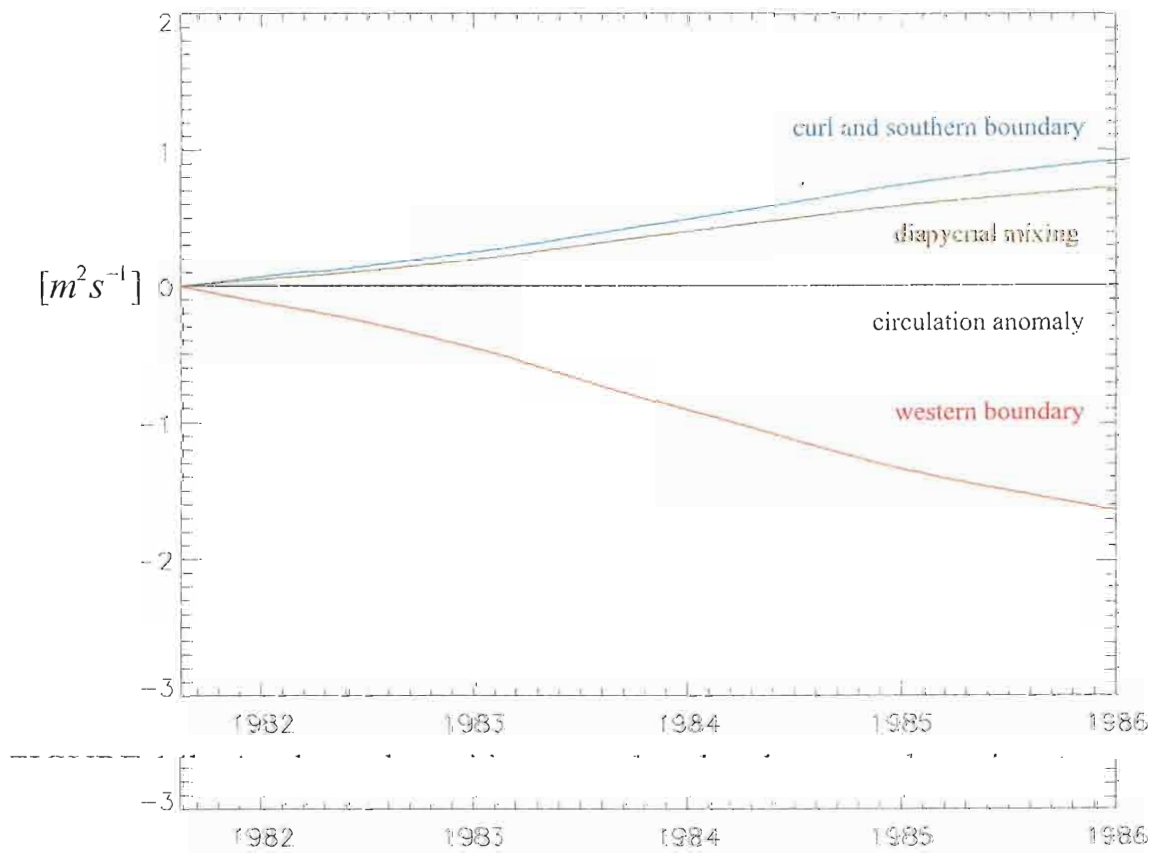
FIGURE 14b: As above, but with summed curl and western boundary terms.

5. SUMMARY AND CONCLUSIONS

A high-resolution numerical ocean model is used to examine the interannual variability of upper ocean vorticity balances in the Gulf of Alaska. The circulation equation, which expresses these balances as derived quantities of model variables, is derived from the model equations of motion. Each term in the equation represents a different pathway through which vorticity can flow. A discretized version of the equation is solved with gridded model output fields, and a time series of the solution of each term constructed.

The solutions show that interannual variability in vorticity balances is predominantly due to atmospheric and oceanic teleconnections originating with the El Niño-Southern Oscillation. The amount of vorticity injected into the upper ocean by the wind stress curl is reduced during the early phase of El Niño events by the weakening of the Aleutian Low [*Emery and Hamilton,* 1985; *Putman,* 1998]. El Niño events also excite poleward-traveling downwelling coastal Kelvin waves that propagate up the eastern continental margin of the northeast Pacific Ocean [*Meyers et al.,* 1998]. These waves strengthen the Alaska Current at the peak of its annual cycle, triggering baroclinic instabilities which result in the formation of a coast-wide train of anticyclonic eddies [*Melsom et al.,* 1995; 1998]. The more southerly of these eddies propagate to the southwest, carrying negative vorticity out of the Gulf of Alaska. This net gain of vorticity is inversely correlated with 1998]. The more southerly of these eddies propagate to the southwest, carrying negative vorticity out of the Gulf of Alaska. This net gain of vorticity is inversely correlated with and serves to balance the nearly contemporaneous reduction of vorticity input by the

37

wind stress curl. Due to the baroclinic nature of both the eddies and the influence of the wind stress curl, the effect is largely confined to the upper ocean.

APPENDIX A. SYMBOLS

Symbol	Definition

A_H coefficient of isopycnal eddy viscosity;

$C(0)$ circulation at the first data record;

$C(t)$ circulation;

C_k coefficient of interfacial friction;

C_b coefficient of bottom friction;

$D(x,y)$ total ocean depth at rest;

f Coriolis parameter;

g acceleration due to gravity;

$$G_{kl} = g \qquad\qquad l \geq k$$

$$G_{kl} = g - g\frac{\rho_k - \rho_l}{\rho_0} \quad l < k;$$

h_k k-th layer thickness;

h_k^+ k-th layer thickness at which entrainment starts;

h_k^- k-th layer thickness at which detrainment starts;

H_k k-th layer thickness at rest;

$$H_k = D(x,v) - \sum_{n=1}^{n-1} H_{l,\ldots} \quad \ldots \text{n-th layer thickness at rest;}$$

$$H_n = D(x,y) - \sum_{l=1}^{n-1} H_l \qquad \text{n-th layer thickness at rest;}$$

$\hat{i}, \hat{j}, \hat{k}$ — zonal, meridional, and vertical unit vectors;

n — number of isopycnal layers;

t — time;

$\vec{v}_k$ — k-th layer velocity;

$V_k = h_k \vec{v}_k$ — k-th layer transport;

ρ_k — k-th layer density, constant in space and time;

ρ_0 — reference density, constant in space and time;

$\vec{\tau}_w$ — wind stress;

$\vec{\tau}_w = \vec{\tau}_k$ — for $k = 0$

$\vec{\tau}_w = C_k \rho_0 |\vec{v}_k - \vec{v}_{k+1}|(\vec{v}_k - \vec{v}_{k+1})$ — for $k = 1 \ldots n\text{-}1$

$\vec{\tau}_w = C_b \rho_0 |\vec{v}_n| \vec{v}_n$ — for $k = n$;

$\omega_k = 0$ — for $k = 0, n$

$\omega_k = \max(0, \omega_k^+) - \max(0, \omega_k^-) - h_k \hat{\omega}_k$ — for $k = 1 \ldots n\text{-}1$;

$$\omega_k^+ = \tilde{\omega}_k \frac{h_k^+}{4}\left(\frac{1}{h_h} - \frac{1}{h_k^+}\right);$$

$$\omega_k^- = \tilde{\omega}_k \frac{h_k^+}{4}\left(\frac{1}{h_k^- + h_k^+ - h_h} - \frac{1}{h_k^+}\right);$$

$$\hat{\omega}_k = \frac{\iint(\max(0, \omega_k^+) - \max(0, \omega_k^-))}{\iint H_k}$$ — global mixing balance term;

$\tilde{\omega}_k$ — k-th level interface reference vertical mixing velocity;

$\tilde{\omega}_k$ — k-th level interface reference vertical mixing velocity;

ζ — vorticity, $\nabla \times \tilde{u}$;

APPENDIX B. DERIVATION OF THE CIRCULATION EQUATION

Consider the equations of motion for the upper layer of an n-layer finite depth model, neglecting the entrainment/detrainment terms.

$$\frac{\partial \vec{V}}{\partial t} + (\nabla \bullet \vec{V} + \vec{V} \bullet \nabla)\vec{v} + \hat{k} \times f\vec{V} = -h\sum_{l=1}^{n}\nabla(h_l - H_l) + \frac{\vec{\tau}_w}{\rho_0} + A_H h\nabla^2\vec{v}$$

$$\frac{\partial h}{\partial t} + \nabla \bullet \vec{V} = 0$$

Expand the first term.

$$\frac{\partial h}{\partial t}\vec{v} + h\frac{\partial \vec{v}}{\partial t} + (\nabla \bullet \vec{V} + \vec{V} \bullet \nabla)\vec{v} + \hat{k} \times f\vec{V} = -h\sum_{l=1}^{n}\nabla(h_l - H_l) + \frac{\vec{\tau}_w}{\rho_0} + A_H h\nabla^2\vec{v}$$

First and third terms cancel via continuity equation.

$$h\frac{\partial \vec{v}}{\partial t} + (\vec{V} \bullet \nabla)\vec{v} + \hat{k} \times f\vec{V} = -h\sum_{l=1}^{n}\nabla(h_l - H_l) + \frac{\vec{\tau}_w}{\rho_0} + A_H h\nabla^2\vec{v}$$

Expand second term with vector identity $(\vec{v} \bullet \nabla)\vec{v} = \frac{1}{2}\nabla^2 v - \vec{v} \times \nabla \times \vec{v}$.

$$h(\frac{\partial \vec{v}}{\partial t} + \frac{1}{2}\nabla^2 v - \vec{v} \times \nabla \times \vec{v}) + \hat{k} \times f\vec{V} = -h\sum_{l=1}^{n}\nabla(h_l - H_l) + \frac{\vec{\tau}_w}{\rho_0} + A_H h\nabla^2\vec{v}$$

Divide by h.

$$(\frac{\partial \vec{v}}{\partial t} + \frac{1}{2}\nabla^2 v - \vec{v} \times \nabla \times \vec{v}) + h^{-1}(\hat{k} \times f\vec{V}) = -\sum_{l=1}^{n}\nabla(h_l - H_l) + \frac{\vec{\tau}_w}{\rho_0 h} + A_H \nabla^2\vec{v}$$

Take the curl. The time derivative in the first term can be taken outside the curl because the curl is a temporally invariant operator.

Take the curl. The time derivative in the first term can be taken outside the curl because the curl is a temporally invariant operator.

$$\frac{\partial}{\partial t}(\nabla \times \vec{v}) + \nabla \times \frac{1}{2}\nabla^2 v - \nabla \times \vec{v} \times \nabla \times \vec{v} + \nabla \times h^{-1}(\hat{k} \times f\vec{V}) =$$

41

$$\nabla \times -\sum_{l=1}^{n} \nabla(h_l - H_l) + \nabla \times \frac{\vec{\tau}_w}{\rho_0 h} + \nabla \times A_H \nabla^2 \vec{v}$$

The second and fifth terms vanish because the curl of a gradient is zero ($\nabla \times \nabla \varphi = 0$), where φ is any scalar.

$$\frac{\partial}{\partial t}(\nabla \times \vec{v}) - \nabla \times \vec{v} \times \nabla \times \vec{v} + \nabla \times h^{-1}(\hat{k} \times f\vec{V}) = \nabla \times \frac{\vec{\tau}_w}{\rho_0 h} + \nabla \times A_H \nabla^2 \vec{v}$$

Use the vector identity $\nabla \times (\vec{A} \times \vec{B}) = (\vec{B} \bullet \nabla)\vec{A} - \vec{B}(\nabla \bullet \vec{A}) - (\vec{A} \bullet \nabla)\vec{B} + \vec{A}(\nabla \bullet \vec{B})$ to expand the second term, where $\vec{A} = \vec{v}$ and $\vec{B} = \nabla \times \vec{v} = \vec{\zeta} = \zeta\hat{k}$.

$$\frac{\partial \vec{\zeta}}{\partial t} - \left[(\zeta\hat{k} \bullet \nabla)\vec{v} - \zeta\hat{k}(\nabla \bullet \vec{v}) - (\vec{v} \bullet \nabla)\zeta\hat{k} + \vec{v}(\nabla \bullet \zeta\hat{k})\right] + \nabla \times h^{-1}(\hat{k} \times f\vec{V}) =$$

$$\nabla \times \frac{\vec{\tau}_w}{\rho_0 h} + \nabla \times A_H \nabla^2 \vec{v}$$

The first term in brackets drops because $(\zeta\hat{k} \bullet \nabla) = \zeta\frac{\partial}{\partial z}$ and $\frac{\partial \vec{v}}{\partial z} = 0$ within the layer. The fourth term in brackets drops because $(\nabla \bullet \zeta\hat{k}) = \frac{\partial \zeta}{\partial z}$, which is zero within the layer.

$$\frac{\partial \vec{\zeta}}{\partial t} + \left[\zeta\hat{k}(\nabla \bullet \vec{v}) + (\vec{v} \bullet \nabla)\zeta\hat{k}\right] + \nabla \times h^{-1}(\hat{k} \times f\vec{V}) = \nabla \times \frac{\vec{\tau}_w}{\rho_0 h} + \nabla \times A_H \nabla^2 \vec{v} \qquad (1)$$

Next simplify the Coriolis and diffusion terms and substitute the results into the above equation. First expand the transport in the Coriolis term and simplify.

$$\hat{k} \times f\vec{V} = \hat{k} \times fh\vec{v} = \begin{vmatrix} \hat{i} & \hat{j} & \hat{k} \\ 0 & 0 & 1 \\ fhu & fhv & 0 \end{vmatrix} = -fhv\hat{i} + fhu\hat{j}$$

$$h^{-1}(\hat{k} \times fh\vec{v}) = -fv\hat{i} + fu\hat{j}$$

$$\nabla \times h^{-1}(\hat{k} \times fh\vec{v}) = \begin{vmatrix} \hat{i} & \hat{j} & \hat{k} \\ \frac{\partial}{\partial x} & \frac{\partial}{\partial y} & \frac{\partial}{\partial z} \\ -fv & fu & 0 \end{vmatrix} = -\hat{i}(\frac{\partial}{\partial z}(fu)) - \hat{j}(\frac{\partial}{\partial z}(fv)) + \hat{k}(\frac{\partial}{\partial x}(fu) + \frac{\partial}{\partial y}(fv))$$

$$\begin{vmatrix} \partial x & \partial y & \partial z \\ -fv & fu & 0 \end{vmatrix} \qquad \partial z \qquad \partial z \qquad \partial x \qquad \partial y$$

The horizontal components are zero because fu and fv don't vary with z within the layer. Recast the vertical component in vectoral format.

$$\nabla \times h^{-1}(\hat{k} \times fh\vec{v}) = \hat{k}(\nabla \bullet f\vec{v})$$

Expand the result using the vector identity $\nabla \bullet c\vec{A} = c(\nabla \bullet \vec{A}) + \vec{A} \bullet \nabla c$, where c is any scalar and $\vec{A}$ is any vector.

$$\nabla \times h^{-1}(\hat{k} \times fh\vec{v}) = \left(f(\nabla \bullet \vec{v}) + \vec{v} \bullet \nabla f\right)\hat{k} \tag{2}$$

Next expand the diffusion term.

$$\nabla \times A_H \nabla^2 \vec{v} = A_H \nabla \times \nabla^2 \vec{v} = A_H(\nabla \times \nabla^2 u)\hat{i} + A_H(\nabla \times \nabla^2 v)\hat{j} = A_H \nabla \times (\nabla^2 u\hat{i} + \nabla^2 v\hat{j}) =$$

$$A_H \begin{vmatrix} \hat{i} & \hat{j} & \hat{k} \\ \dfrac{\partial}{\partial x} & \dfrac{\partial}{\partial y} & \dfrac{\partial}{\partial z} \\ \nabla^2 u & \nabla^2 v & 0 \end{vmatrix} = -\hat{i}A_H \frac{\partial}{\partial z}\nabla^2 v + \hat{j}A_H \frac{\partial}{\partial z}\nabla^2 u + \hat{k}A_H(\frac{\partial}{\partial x}\nabla^2 v - \frac{\partial}{\partial y}\nabla^2 u)$$

$\nabla^2 u$ and $\nabla^2 v$ do not vary with z within the layer, therefore the horizontal terms are zero.

$$\nabla \times A_H \nabla^2 \vec{v} = \hat{k}A_H(\nabla^2 v_x - \nabla^2 u_y) = \hat{k}A_H\left(\nabla^2(v_x - u_y)\right) = \hat{k}A_H(\nabla^2 \zeta) \tag{3}$$

Substitute new Coriolis (2) and diffusion (3) expressions into equation (1).

$$\frac{\partial \zeta}{\partial t}\hat{k} + \left[\zeta(\nabla \bullet \vec{v}) + (\vec{v} \bullet \nabla)\zeta\right]\hat{k} + \left(f(\nabla \bullet \vec{v}) + \vec{v} \bullet \nabla f\right)\hat{k} = \nabla \times \frac{\vec{\tau}_w}{\rho_0 h} + \hat{k}A_H(\nabla^2 \zeta) \tag{4}$$

Combine terms 2 with 4 and 1 with 3.

$$\frac{\partial \zeta}{\partial t}\hat{k} + (\zeta + f)(\nabla \bullet \vec{v})\hat{k} + (\vec{v} \bullet \nabla)(\zeta + f)\hat{k} = \nabla \times \frac{\vec{\tau}_w}{\rho_0 h} + A_H(\nabla^2 \zeta)\hat{k}$$

$$\frac{\partial \zeta}{\partial t}\hat{k} + (\nabla \bullet \vec{v} + \vec{v} \bullet \nabla)(\zeta + f)\hat{k} = \nabla \times \frac{\vec{\tau}_w}{\rho_0 h} + A_H(\nabla^2 \zeta)\hat{k} \tag{5}$$

Take the surface integral of equation (5), where D is the domain of integration.

$$\int_D (5) \bullet d\vec{A} = \int_D (5) \bullet \hat{n}dA = \int_D (5) \bullet \hat{k}dA$$

$$\int_D \frac{\partial \zeta}{\partial t}dA + \int_D (\nabla \bullet \vec{v} + \vec{v} \bullet \nabla)(\zeta + f)dA = \int_D (\hat{k} \bullet \nabla \times \frac{\vec{\tau}_w}{\rho_0 h})dA + A_H \int_D (\nabla^2 \zeta)dA \tag{6}$$

$$\int_D \frac{\partial \zeta}{\partial t}dA + \int_D (\nabla \bullet \vec{v} + \vec{v} \bullet \nabla)(\zeta + f)dA = \int_D (\hat{k} \bullet \nabla \times \frac{\vec{\tau}_w}{\rho_0 h})dA + A_H \int_D (\nabla^2 \zeta)dA \tag{6}$$

Stokes' Theorem states that $\int_D (\nabla \times \vec{v}) \bullet d\vec{A} = \int_{\partial D} \vec{v} \bullet d\vec{s} = C$, where C is the circulation.

Move the time derivative out of the integral in the first term of equation (6) and substitute the Stoke's expression, recalling that $\nabla \times \vec{v} = \zeta$.

$$\frac{\partial C}{\partial t} = -\int_D (\nabla \bullet \vec{v} + \vec{v} \bullet \nabla)(\zeta + f)dA + \int_D (\hat{k} \bullet \nabla \times \frac{\vec{\tau}_w}{\rho_0 h})dA + A_H \int_D (\nabla^2 \zeta)dA \qquad (7)$$

Simplify the first term on the right-hand side of (7).

$$-\int_D (\nabla \bullet \vec{v} + \vec{v} \bullet \nabla)(\zeta + f)dA = -\int_D (u_x + v_y + u\frac{\partial}{\partial x} + v\frac{\partial}{\partial y})(\zeta + f)dA =$$

$$-\int_D [u_x(\zeta + f) + v_y(\zeta + f) + u(\zeta + f)_x + v(\zeta + f)_y]dA =$$

$$-\int_D \left[\frac{\partial}{\partial x}(u(\zeta + f)) + \frac{\partial}{\partial y}(v(\zeta + f))\right]dA \qquad (8)$$

$\int_D (M_x - N_y)dA = \oint_{\partial D} Ndx + Mdy$ is an alternate formulation of Stokes' theorem. Letting $M = u(\zeta + f)$ and $N = -v(\zeta + f)$ sets the left-hand side of Stokes' theorem equal to equation (8).

$$-\int_D (\nabla \bullet \vec{v} + \vec{v} \bullet \nabla)(\zeta + f)dA = -\oint_{\partial D} u(\zeta + f)dy - v(\zeta + f)dx$$

Let the Domain D be a box approximating the Gulf of Alaska, .with closed boundaries on the northern and eastern sides. Therefore $u = 0$ on the eastern boundary and $v = 0$ on the northern boundary. Carry out the line integral counterclockwise from the northwest vertex. Integration limits will be denoted by 'NW' for the northwest vertex of the box, etc.

$$-\int_D (\nabla \bullet \vec{v} + \vec{v} \bullet \nabla)(\zeta + f)dA =$$

$$-\int_{NW}^{SW} u(\zeta + f)dy + \int_{SW}^{SE} v(\zeta + f)dx - \int_{SE}^{NE} u(\zeta + f)dy + \int_{NE}^{NW} v(\zeta + f)dx$$

The third and fourth integrals on the right-hand side vanish because $u = 0$ on the eastern boundary and $v = 0$ on the northern boundary. Reverse the direction of integration of the first integral in order that the sense of integration be positive.

boundary and $v = 0$ on the northern boundary. Reverse the direction of integration of the first integral in order that the sense of integration be positive.

$$-\int_D (\nabla \bullet \vec{v} + \vec{v} \bullet \nabla)(\zeta + f)dA = \int_{SW}^{NW} u(\zeta + f)dy + \int_{SW}^{SE} v(\zeta + f)dx \qquad (9)$$

44

Substitute (9) into equation (7).

$$\frac{\partial C}{\partial t} = \int\limits_{SW}^{NW} u(\zeta + f)dy + \int\limits_{SW}^{SE} v(\zeta + f)dx + \int\limits_{D}(\hat{k} \bullet \nabla \times \frac{\vec{\tau}_w}{\rho_0 h})dA + A_H \int\limits_{D}(\nabla^2 \zeta)dA \qquad (10)$$

Integrate equation (10) with respect to time from $t = 0$ to t. Use the fundamental theorem of calculus to simplify the left-hand side. The result is the circulation equation.

$$C(t) - C(0) =$$

$$\int\limits_{0}^{t}\int\limits_{SW}^{NW} u(\zeta + f)dydt + \int\limits_{0}^{t}\int\limits_{SW}^{SE} v(\zeta + f)dxdt + \int\limits_{0}^{t}\int\limits_{D}(\hat{k} \bullet \nabla \times \frac{\vec{\tau}_w}{\rho_0 h})dAdt + A_H \int\limits_{0}^{t}\int\limits_{D}(\nabla^2 \zeta)dAdt$$

REFERENCES

Chelton, D.B., and R.E. Davis, Monthly mean sea-level variability along the west coast of North America, *J. Phys. Oceanogr.*, 12, 757-784, 1982.

Clarke, A.J., The reflection of equatorial waves from oceanic boundaries, *J. Phys. Oceanogr.*, 13, 1193-1207, 1983.

Cummins, P.F., and H.J. Freeland, Observations and Modeling of Wind-driven Currents in the Northeast Pacific, *J. Phys. Oceanogr.*, 23, 488-502, 1993.

Donohue, K.A., Wimbush, M., Zhu, X., Chiswell, S.M., Lukas, R., Miller, L., and H.E. Hurlburt, Five years' central Pacific sea level from in-situ array, satellite altimeter, and numerical model, *Atmos.-Ocean*, 32, 495-506, 1994.

Emery, W.J., and K. Hamilton, Atmospheric Forcing of Interannual Variability in the Northeast Pacific Ocean: Connections with El Niño, *J. Geophysic. Res.*, 90, 857-868, 19985.

Enfield, D.B., and J.S. Allen, On the structure and dynamics of monthly mean sea level anomalies along the Pacific coast of North and South America, *J. Phys. Oceanogr.*, 10, 557-578, 1980.

Hellerman, S., and M. Rosenstein, Normal monthly wind stress over the world ocean with error estimates, *J. Phys. Oceanogr.*, 13, 1093-1104, 1983.

Hogan, P.J., Hurlburt, H.E., Jacobs, G.A., Wallcraft, A.J., Teague, W.J., and J.L. Pringle, Simulation of GEOSAT, TOPEX/Poseidon, and ERS-1 altimeter data from a $1/8^o$ Pacific Ocean Model: Effects of space-time resolution on mesoscale sea surface height variability, *Mar. Technol. Soc. J.*, 26(2), 98-107, 1992.

Hurlburt, H. E., and J. D. Thompson, A numerical study of the Loop current intrusions and eddy-shedding, *J. Phys. Oceanogr.*, 10, 1611-1651, 1980.

Hurlburt, H.E., Wallcraft, A.J., Sirkes, Z., and E.J. Metzger, Modeling of the Global and Pacific Oceans: On the path to eddy-resolving ocean prediction, *Oceanography*,

Hurlburt, H.E., Wallcraft, A.J., Sirkes, Z., and E.J. Metzger, Modeling of the Global and Pacific Oceans: On the path to eddy-resolving ocean prediction, *Oceanography*, 5, 9-18, 1992.

Hurlburt, H.E., Hogan, P.J., Metzger, E.J., Schmitz, W.J., and A.J. Wallcraft, Dynamics of the Kuroshio/Oyashio current system using eddy-resolving models of the North Pacific Ocean, *J. Geophys. Res.*, 101, 941-976, 1996.

Jacobs, G.A., Hurlburt, H.E., Kindle, J.C., Metzger, E.J., Mitchell, J.L., Teague, W.J., and A.J. Wallcraft, Decade-scale trans-Pacific propagation and warming effects of an El Nino anomaly, *Nature*, 370, 360-363, 1994.

Jacobs, G.A., Teague, W.J., Mitchell, J.L., and H.E. Hurlburt, An examination of the North Pacific Ocean in the spectral domain using GEOSAT altimeter data and a $1/8^o$ 6-layer Pacific Ocean Model, *J. Geophysic. Res.*, 101, 1025-1044, 1996.

Kindle, J.C., and P.A. Phoebus, The ocean response to operational westerly wind bursts during the 1991-1992 El Nino, *J. Geophysic. Res.*, 100, 4893-4920, 1995.

Leonardi, A.P., Dynamics of the North Hawaiian Ridge Current, Master's Thesis, Florida State University, 1998.

Levitus, S., Climatological atlas of the World Ocean, *NOAA Professional Paper-13*, 173 pp., 1982.

Melsom, A., Hurlburt, H.E., Metzger, E.J., Meyers, S.D., and J.J. O'Brien, El Nino induced Eddies in the Gulf of Alaska, submitted to *Science*, August, 1995.

Melsom, A., Meyers, S.D., Hurlburt, H.E., Metzger, E.J., and J.J. O'Brien, 1999: ENSO Effects on Gulf of Alaska Eddies, Earth Interactions, 3. [Available at http://EarthInteractions.org]

Messinger, F. and A. Arakawa, *Numerical Methods used in Atmospheric Models*, GARP Publ. Serv., World Meteorological Organization, 64 pp., 1976.

Metzger, E.J., Hurlburt, H.E., Kindle, J.C., Sirkes, Z., and J. Pringle, Hindcasting of wind-driven anomalies using a reduced gravity global ocean model, *J. Mar. Technol. Soc.*, 26(2), 23-32, 1992.

Metzger, E.J., Hurlburt, H.E., Jacobs, G.A., and J.C. Kindle, Hindcasting of wind-driven anomalies using reduced gravity global ocean models with $1/2^o$ and $1/4^o$ resolution, NRL Tech. Rep. 9444, 21 pp., Nav. Res. Lab, Stennis Space Center, Miss., 1994.

Metzger, E.J., and H.E. Hurlburt, Coupled dynamics of the South China Sea, the Sulu Sea and the Pacific Ocean, *J. Geophysic. Res.*, 101, 12,331-12,352, 1996.

Metzger, E.J., and H.E. Hurlburt, Coupled dynamics of the South China Sea, the Sulu Sea and the Pacific Ocean, *J. Geophysic. Res.*, 101, 12,331-12,352, 1996.

Meyers, S.D., and S. Basu, Eddies in the eastern Gulf of Alaska from TOPEX/Poseidon altimetry, submitted to *J. Geophys. Res.* September 1997, revised May 1998.

Meyers, S.D., Melson, A., Mitchum, G., and J.J. O'Brien, Detection of the fast Kelvin Wave teleconnection due to El Niño-Southern Oscillation, *J. Geophys. Res.*, 103, 27,665-27,663, 1998.

Mitchell, J.L., Teague, W.J., Jacobs, G.A., and H.E. Hurlburt, Kuroshio Extension dynamics from satellite altimetry and a model simulation, *J. Geophys. Res.*, 101, 1045-1058, 1996.

Mitchum, G.T., The source of 90-day oscillations at Wake Island, *J. Geophys. Res.*, 100, 2459-2475, 1995.

NOAA, ETOP05 digital relief of the earth, Natl. Geophys. Data Cent., Washington, D.C., Data Announc. 86-MGG-07, 1986.

Putman, W.M., Assimilation of FSU and NCEP Reanalysis Pseudostress Products over the Pacific Ocean and Complex EOF Analysis of the Resulting Fields, Master's Thesis, Florida State University, 1998.

Shriver, J.F., and H.E. Hurlburt, The Contribution of the Global Thermohaline Circulation to the Pacific to Indian Ocean Throughflow via Indonesia, *J. Geophysic. Res.*, 102, 5491-5511, 1997.

Thomson, R.E., On the Alaskan Stream, *J. Phys. Oceanogr.*, 2, 363-371, 1972.

Thomson, R.E., and J.F. Gower, A basin-scale oceanic instability event in the Gulf of Alaska, *J. Geophysic. Res.*, 103, C2, 3033-3040, 1998.

Wallcraft, A.J., *The Navy Layered Ocean Model User's Guide*, Naval Research Laboratory, Stennis Space Center, Mississippi, 21 pp., 1991.

BIOGRAPHICAL SKETCH

I was born in Baton Rouge, Louisiana on 29 January 1968. I spent a happy childhood there and was very fortunate in my parents' insistence on getting a good education. I credit Carl Sagan's wonderful television series *Cosmos* and Aleksandr Solzhenitsyn's The Gulag Archipelago for stimulating an early interest in understanding the surrounding larger world and thereby drawing me onto my current path.

After years of vocational indecision over whether to pursue physical or political science, I graduated in August 1993 with a BS in Physics and a minor in political science. After several ungratifying years in the modern temporary workforce, I decided to pursue my interest in climate change by studying oceanography at Florida State University. My experience at the Center for Ocean - Atmospheric Prediction Studies has left me with a deep appreciation of mankind's ability to utilize knowledge of the mathematical understructure of reality to divine the past and future. I remain, however, an avid hobbyist of political theory, foreign affairs, and strategic simulation.